

# A 37-40 GHz Dual-Polarized 16-Element Phased-Array Antenna with Near-Field Probes

by

Ziran He

A thesis  
presented to the University of Waterloo  
in fulfillment of the  
thesis requirement for the degree of  
Master of Applied Science  
in  
Electrical and Computer Engineering

Waterloo, Ontario, Canada, 2022

© Ziran He 2022

## **Author's Declaration**

I hereby declare that I am the sole author of this thesis. This is a true copy of the thesis, including any required final revisions, as accepted by my examiners.

I understand that my thesis may be made electronically available to the public.

## Abstract

With the development of fifth-generation (5G) communication networks, in order to meet the growing demand for high-speed and low-latency wireless communication services, channel capacity has become the main driving force for choosing millimeter wave (mm-wave) over over-crowded sub-6 GHz frequency bands. Recently, beamforming phased array attracts significant research efforts as it is a promising solution and unique in its ability to overcome the high path-loss at high frequency, provide fast beam steering and deliver better user-ends experience. However, to alleviate the issues that associated with beamforming phased array, such as imbalance between array elements and non-linearity caused by power-amplifiers (PAs) in beamforming channels, far-field (FF) based array calibration and digital pre-distortion (DPD) need to be performed, which is not practical in real world scenario.

This thesis presents a low-cost 16-element dual-polarized mm-wave antenna-on-printed circuit board (PCB) transmitter RF beamforming array with embedded near-field probes (NFPs) at 37-40 GHz. The elements are orthogonal, proximity-coupled feed dual-polarized patch antenna with a spacing of  $0.5\lambda$  within  $2 \times 2$  subarray and  $0.6\lambda$  between  $2 \times 2$  subarray at 38.5 GHz, resulting in maximum 17.7 dB gain with a scan angle of  $\pm 50^\circ$ ,  $\pm 20^\circ$  in azimuth and  $\pm 20^\circ$ ,  $\pm 50^\circ$  in elevation for vertical polarization and horizontal polarization, respectively. Without affecting phased array performance, the NFPs achieve flat and comparable coupling magnitude and group delay to the closet RF chain for both polarizations, across operating frequency range. This ensures the quality of received output signal from phased array to implement array calibration and DPD. The configuration of embedded NFPs maintains the scalability of phased array and eliminate the needs of impractical FF reference probe for array calibration and DPD.

## Acknowledgements

I would like to mostly thank my parents, Mengyun He and Xiaoyan Li, for their unwavering love and encouragement, without whom I would never have become who I am now.

I would like to thank my supervisor, Professor Slim Boumaiza, for providing me with guidance in this research work and the opportunities for being a part of EmRG family for the past three years.

I would like to thank my girlfriend Mingtong Ju for always being there to share both my joy and pain.

I would like to thank Ahmed Ben Ayed, Jingjing Xia and Yushi Cao for not only providing me with the help, but also teaching me the way of thinking, from research to career.

I would like to thank Bernard Tung and Huixin Jin for participating my research work while bearing with my daily nagging.

Last but not least, I would like to thank all EmRG colleagues for their friendship and mentorship.

# Table of Contents

List of Figures	vii
List of Tables	xi
<b>1 Introduction</b>	<b>1</b>
1.1 Motivation . . . . .	1
1.2 Problem Statement . . . . .	3
1.3 Thesis Organization . . . . .	5
<b>2 Background Theory and Literature Review</b>	<b>6</b>
2.1 Background Theory . . . . .	6
2.2 Literature on RF Beamforming Array Construction Below 100 GHz . . . . .	11
2.2.1 Antenna-on-PCB . . . . .	11
2.2.2 Antenna-in-Package . . . . .	14
2.2.3 Antenna-on-Chip . . . . .	19
2.2.4 Comparison . . . . .	21
2.3 Literature on Transmitter Observation Receiver . . . . .	23
2.4 Discussion . . . . .	29

<b>3</b>	<b>37-40 GHz 16-Element Dual-Polarized RF Beamforming Phased Array Design</b>	<b>30</b>
3.1	Project Scope . . . . .	30
3.2	Antenna Design . . . . .	31
3.2.1	Feeding Mechanism . . . . .	33
3.2.2	PCB Stackup . . . . .	34
3.2.3	Dual-Polarized Patch Antenna . . . . .	37
3.3	Array Design . . . . .	40
3.3.1	Decoupling Structure . . . . .	41
3.3.2	Near-Field Probe . . . . .	51
<b>4</b>	<b>Experimental Validation</b>	<b>56</b>
4.1	Measurement Setup . . . . .	56
4.2	Beamforming Array Assessment . . . . .	57
4.2.1	Array Calibration . . . . .	57
4.2.2	Frequency Response . . . . .	59
4.2.3	Radiation Pattern . . . . .	59
<b>5</b>	<b>Conclusion and Future Works</b>	<b>65</b>
5.1	Conclusion . . . . .	65
5.2	Future Works . . . . .	66
	<b>References</b>	<b>68</b>

# List of Figures

1.1	Major wireless technologies on radio wave spectrum [1] . . . . .	2
1.2	Download speeds comparison of Sub-6GHz and mm-wave [2] . . . . .	3
2.1	Concept of phased array . . . . .	7
2.2	Beamformer in 2-D phased array . . . . .	8
2.3	RF Beamforming Architecture . . . . .	8
2.4	Digital Beamforming Architecture . . . . .	9
2.5	Hybrid Beamforming Architecture . . . . .	10
2.6	A survey of phased array construction choices below 100 GHz [3, 4, 5, 6, 7, 8, 9, 10, 11, 12, 13, 14, 15, 16, 17, 18, 19, 20, 21, 22, 23, 24] . . . . .	12
2.7	(a) Block diagram of the wideband 5G 8×8 phased array. (b) Stackup of low-cost 12-layer PCB. [15] . . . . .	13
2.8	(a) Antenna side of 1024-element Ku-band SATCOM TX array. (b) Chip side of 256-element Ku-band SATCOM TX quadrant. [13] . . . . .	14
2.9	Implemented PCB with patch antenna on the back side [17] . . . . .	15
2.10	(a) Antenna view. (b) Chip view and 8 × 16 phased-array. [14] . . . . .	15
2.11	Demonstrated Antenna-in-Package with LTCC substrate from (a) IBM [25], [26] (b) Intel [7] (c) Samsung [23] . . . . .	16

2.12	(a) Illustration of the antenna-in-package assembly breakout, layer stack-up, antenna feeds, and board-level mounting concept. (b) Top view and bottom view of a fully assembled antenna array package with mounted BGA solder balls and four transceiver ICs. [19]	17
2.13	(a) Base station antenna tile with 4x4 active patch array and 2x4 dummies [20]. (b) Gnb prototype photo [21].	19
2.14	(a) Cross section of high-efficiency differential dipole antenna. (b) Block diagram and photo of bondwire-stitched 256-element phased array board. [12]	20
2.15	Functional block diagram of the four-element array with switch between the output from the receiving over-the-air (OTA) horn antenna and each of the coupled PA lines [27]	24
2.16	(a) Phased-array Tx with DPD using the proposed combined feedback architecture and OTA calibration. (b) Layout picture of the common FB line for eight transmit paths. [28]	25
2.17	Diagrams of over-the-air diversity feedback receivers configuration. (a) Symmetrical diversity feedback receivers configuration. (b) Shared feedback loop. [29]	26
2.18	16-element RF beamforming array with near-field prober receivers placed on array perimeters [30]	27
2.19	Layout illustration of (a) proposed beamforming transmitter with NFPA placed at the center of each 2x2 subarray and (b) four quad-core BFICs (on one module) that feed 16 patch antennas. [31]	27
3.1	Design process of proposed beamforming phased array with embedded near-field probes	31
3.2	Typical Feeds for patch antennas [32]	32
3.3	Routing of (a) coaxial-feed (b) proximity-coupled feed patch antenna	34
3.4	PCB stackup and lamination logic used in project	35

3.5	Top view of (a) initial design (b) final design of unit cell element . . . . .	38
3.6	Simulated (a) input matching (b) port isolation versus frequency . . . . .	39
3.7	Dual-polarized proximity-coupled feed patch antenna design parameter . . .	40
3.8	Overview of 4x4 dual-polarized phased array board with decoupling structure	41
3.9	Geometry of decoupling structure . . . . .	42
3.10	Simulated input matching of 4x4 dual-polarized phased array: (a) with de- coupling structure (b) without decoupling structure . . . . .	43
3.11	Simulated mutual coupling of 4x4 dual-polarized phased array: (a) with decoupling structure (b) without decoupling structure . . . . .	44
3.12	Simulated surface current distribution: (a) with decoupling structure (b) without decoupling structure . . . . .	45
3.13	Simulated Active S-parameters of corner elements. . . . .	46
3.14	Simulated Active S-parameters of edge elements. . . . .	47
3.15	Simulated Active S-parameters of middle elements. . . . .	48
3.16	Simulated radiation pattern at boresight for V-pol @ 38.5 GHz . . . . .	49
3.17	Simulated normalized radiation pattern for H-pol when scanned to $\pm 60^\circ$ @ 38.5 GHz . . . . .	50
3.18	Overview of 4x4 dual-polarized phased array board with NFPs . . . . .	52
3.19	Simulated magnitude and group delay of coupling between NFP and sur- rounding antenna elements . . . . .	54
3.20	Simulated NMSE and EVM of received modulated signal from NFPs . . . .	55
4.1	CW Measurement setup . . . . .	57
4.2	Gain variation before and after calibration . . . . .	58
4.3	Phase variation after calibration . . . . .	59
4.4	VNA S-parameters measurements . . . . .	60

4.5	Measured pattern at boresight in horizontal plane at 38.5 GHz . . . . .	61
4.6	Measured pattern with $-60^\circ$ to $60^\circ$ for V-pol in horizontal plane at 38.5 GHz	62
4.7	Measured pattern with $-20^\circ$ to $20^\circ$ for H-pol in horizontal plane at 38.5 GHz	64

# List of Tables

2.1	Comparison of various approaches of phased array construction. . . . .	22
3.1	Purposes of each type of via in PCB stackup. . . . .	37
3.2	Summary of design parameter of dual-polarized unit cell patch antenna. . .	40
3.3	Detail of modulated signal used in simulation. . . . .	53

# Chapter 1

## Introduction

### 1.1 Motivation

Wireless communication has profoundly changed people's lives for the past decades. In order to cope with the explosive data traffic growth, massive device connections and continuously surged new business scenarios (e.g. The Internet of Things market is forecast to grow from an installed base of 15.4 billion devices in 2015 to 75.4 billion in 2025 [33]), the fifth-generation mobile communications system came into being. It is well known that spectrum is the most important but scarce resource in the 5G era, there are two major types of frequency ranges have been assigned to 5G: Sub-6 GHz and mm-wave.

Compared with the frequency bands below 6 GHz, which is very crowded and has been already occupied by many existing applications (Fig. 1.1), the mm-wave frequency band still waits to be explored and utilized. The biggest advantage of the mm-wave band is its high speed and high bandwidth. Frequency are like carriages, the higher the frequency, the more carriages, and the more information can be loaded within the same time. In theory, the sub-6 GHz band system can use a maximum bandwidth of 100 MHz and a maximum data transfer rate of 1 Gbps; while the mm-wave band can provide a large available bandwidth above 800 MHz, so it can support a peak data rate of several Gbps. In fact, as indicated in Fig. 1.2, the actual test result shows that the average mm-wave download

speeds is about 4 times that of the Sub-6 GHz band and the peak download speeds can even reach above 2 Gbps. In the past, mm-wave were mostly used in aerospace industries such as satellites and military. In recent years, due to the requirements of achieving high data rates and low latency real-time operation in many daily life applications, such as artificial intelligence, self-driving cars and high definition streaming, millimeter-wave starts to attract more research efforts than ever.

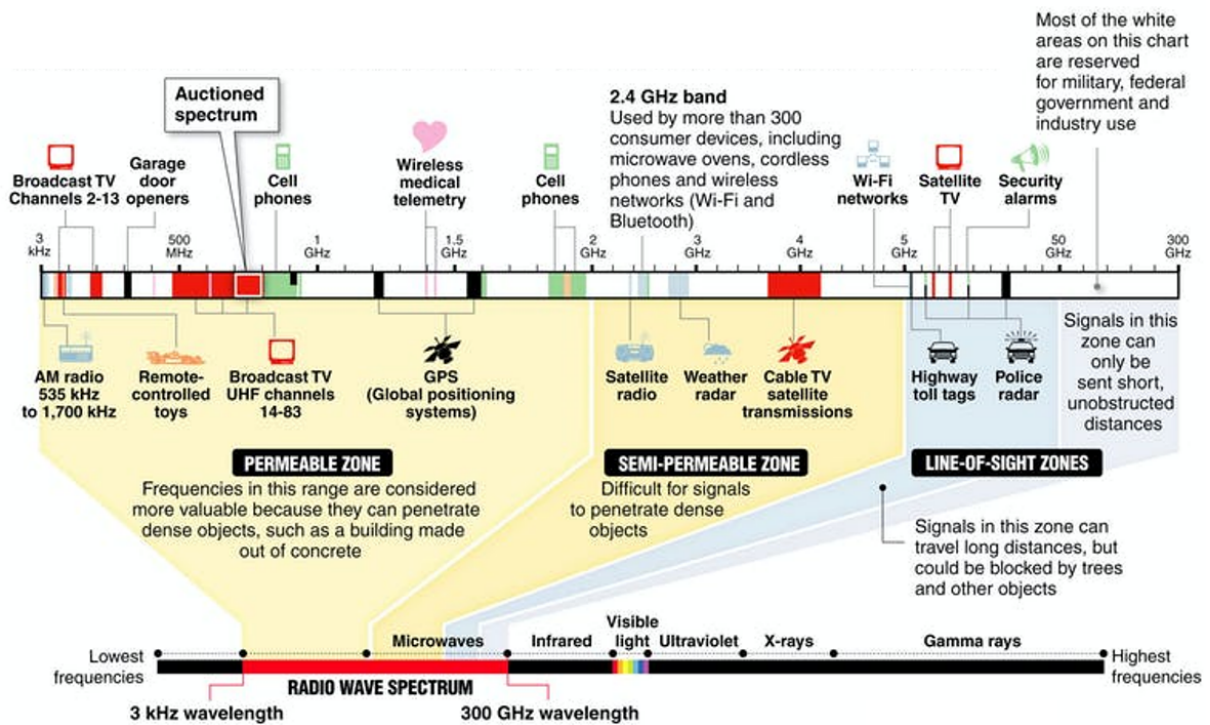


Figure 1.1: Major wireless technologies on radio wave spectrum [1]

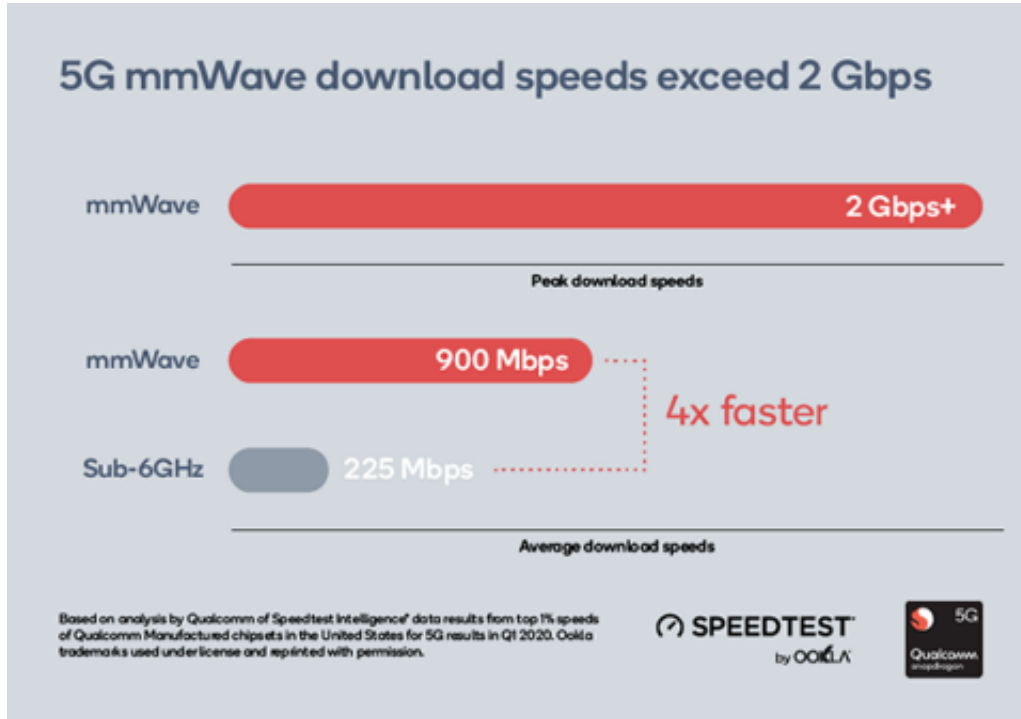


Figure 1.2: Download speeds comparison of Sub-6GHz and mm-wave [2]

## 1.2 Problem Statement

Despite its larger modulation bandwidths thus higher channel capacity than sub-6 GHz systems, many challenges and hardware design complexities arise along with the migration to mmWave frequency bands. The first notable issue is high free-space path loss (FSPL), which can be expressed as:

$$FSPL[dB] = 10 \log_{10} \left[ \left( \frac{4\pi df}{c_0} \right)^2 \right] \quad (1.1)$$

where  $d$  is the distance between transmitter and receiver,  $c_0$  is the speed of light in free space and  $f$  is the carrier frequencies of transmitted signal. Hence, if signal transmits in free space, with fixed distance  $d$ , the higher the frequencies, the higher the FSPL. In other

words, the coverage area of mm-wave transceiver base stations is limited when compared to their sub-6 GHz peers.

Fortunately, beamforming phased array has been proved to be a promising solution to alleviate high FSPL at mm-wave bands. This is because that the antenna gains are proportional to the frequency squared for a fixed physical aperture size, which means transmitter and receiver antenna provide more compensation to the FSPL at higher frequencies. However, 5G mm-wave base station requires more antenna elements to be installed, which makes array calibration more complicated. Ideally, to achieve the precise beamforming to meet 5G communications standard, each element is supposed to transmit or receive the same signal with only phase and magnitude being different. Limited by the manufacture tolerance, the actual antenna array may have a large initial phase error, which will lead to beamforming distortion and seriously affect the signal quality.

To generate higher transmitted power, PAs are the key components in beamforming phased array systems. The 5G new radio (NR) standard specifies orthogonal frequency division multiplexing (OFDM) signal bandwidths up to 100 MHz in sub-6 GHz (Frequency range 1), and up to 400 MHz in mmw-ave (Frequency range 2: 24-53 GHz). While increasing the data rates and the spectral efficiency to the next level, the complex modulation schemes express high peak-to-average power ratios (PAPRs), therefore, lead the use of PAs into dilemma. These high peak-power level drives the PAs exceed their P1dB gain compression point and into non-linear region which causes signal distortion and high bit error rate (BER). This means the PAs require to operate at output power level with great back-off from gain compression point which reduces the transmitted power and suffers from low power-added efficiency (PAE). To tackle this predicament, DPD, a widely implemented linearization technique, applies inverse distortion, using a pre-distorter, at the input signal of the PA to cancel the distortion generated by PAs.

Both array calibration and DPD technique for transmitters require a transmitter observation receiver (TOR) to monitor the transmitter's performance and synthesize the appropriate calibration and DPD function coefficients. Conventionally, a FF reference probe, most of time, a receiver antenna serves as a feedback path to perform array calibration and train DPD function. However, in real-world scenario, setting up FF TOR and performing over-the-air (OTA) DPD and calibration is not always realistic and can be inefficient. As

an attempt to address above-mentioned challenges, this thesis proposes a dual-polarized mm-wave beamforming array with embedded NFPs which eliminates the unpractical FF probe for array calibration and DPD training.

## 1.3 Thesis Organization

This thesis is organized into the following chapters: Chapter 2 first introduces the background theories of beamforming phased array, then reviews related research works in literature, and discusses some observations from prior state-of-art. Chapter 3 presents a 37-40 GHz dual-polarized 16-element transmitter phased-array which includes design details and simulation results. Chapter 4 presents the measurement results of the fabricated prototype. Chapter 5, lastly, concludes this thesis and suggests potential future works.

# Chapter 2

## Background Theory and Literature Review

### 2.1 Background Theory

Unlike bulky and mechanically-steered dish antenna, electrically-steered phased array antennas offers plentiful benefits, such as low profile, multiple beams generation and fast beam angle steering speed. In order to understand how to steer a phased array beam in a more intuitive way, Fig. 2.1 first illustrates  $n$  antenna elements are placed close to each other in one dimension with distance of  $d$ . A coherent time delay is applied to the RF channel of each antenna, which means the first antenna starts to transmit signal at  $0t$ , and the  $n$ th antenna starts to transmit signal at  $n\Delta t$ . By doing so, this coherent combining results in each antenna elements' transmitted wave constructively interfere with others to form a larger signal called the main lobe pointed to the desired angle  $\theta$  to the boresight. Meanwhile, nulls and side lobes are also formed in undesired directions due to the destructive interference. Since electromagnetic waves are sinusoidal, time delay can also be emulated with phase shift which is more practical and precise to control the hardware.

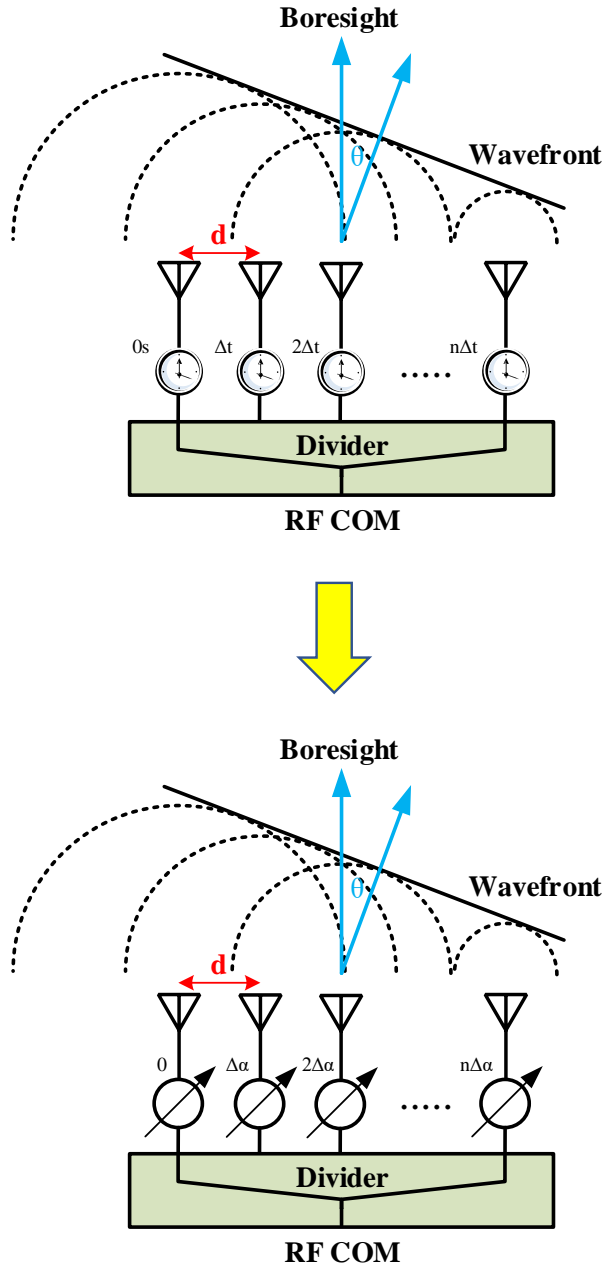


Figure 2.1: Concept of phased array

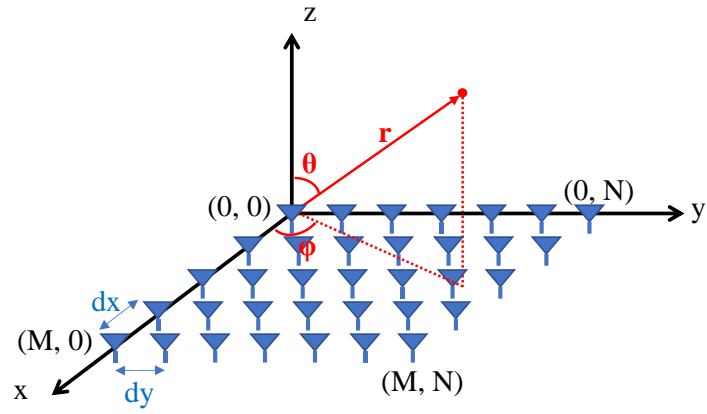


Figure 2.2: Beamformer in 2-D phased array

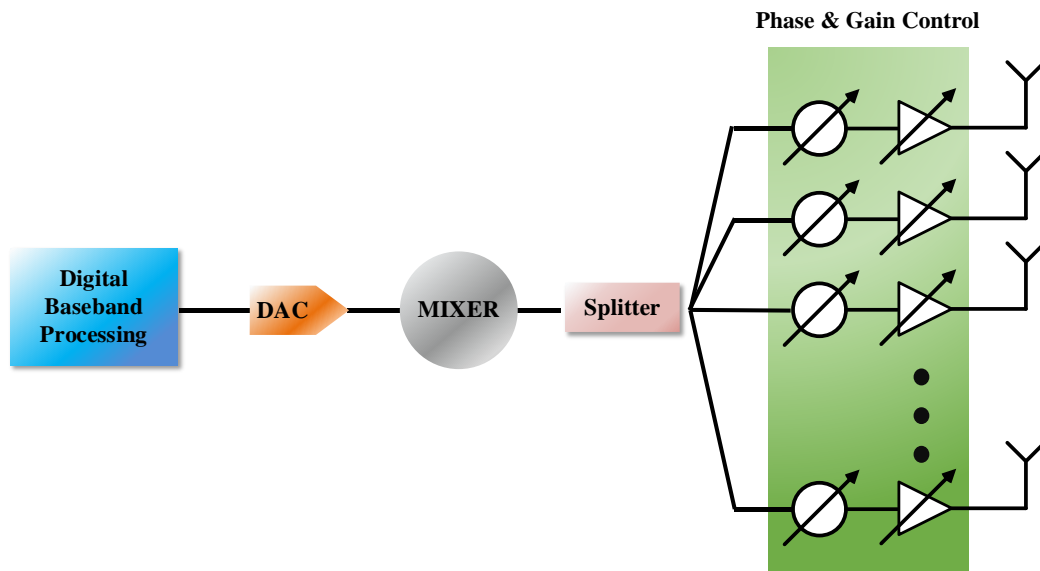


Figure 2.3: RF Beamforming Architecture

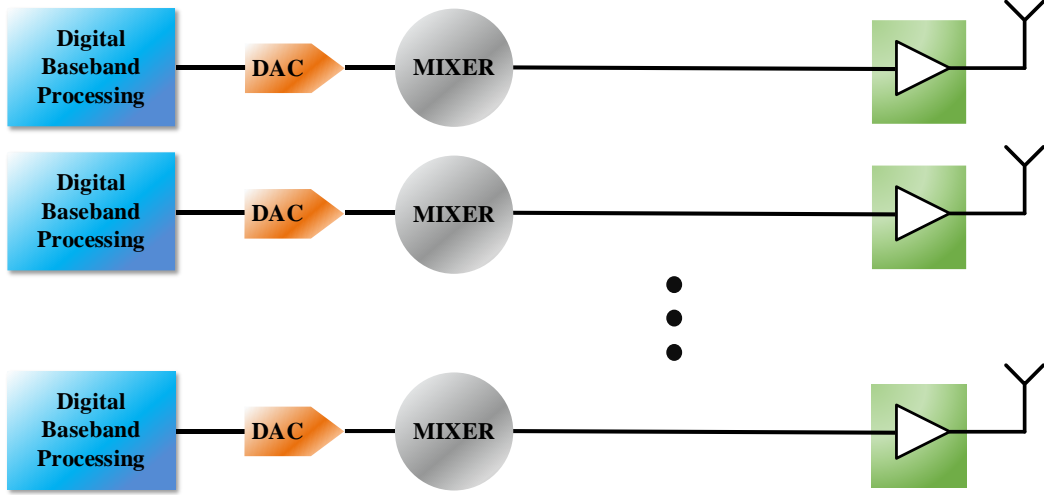


Figure 2.4: Digital Beamforming Architecture

Base on simple trigonometry, one can derive the phase shift equation, given by:

$$\Delta\Phi = \frac{2\pi d \sin\theta}{\lambda} \quad (2.1)$$

From equation 2.1, one can observe, in order to have a full  $180^\circ$  shift between antenna elements so to provide a theoretical  $90^\circ$  beam direction scan capability, the distance  $d$  needs to be equal to half of the signal wavelength  $\lambda/2$ . The same theory can also be applied to two-dimensional phased array, as illustrated in Fig. 2.2, there is an additional beam steering angle of  $\phi$ . Hence, take the antenna element located at origin  $(0,0)$  as reference, the phase shift equation for the element located at  $(M,N)$  unit distance away from the reference element can be given by:

$$PS(M, N) = \frac{\sqrt{M^2 + N^2}}{\lambda} \times \cos(\phi - \arctan(\frac{N}{M})) \times 2\pi \sin(\theta) \quad (2.2)$$

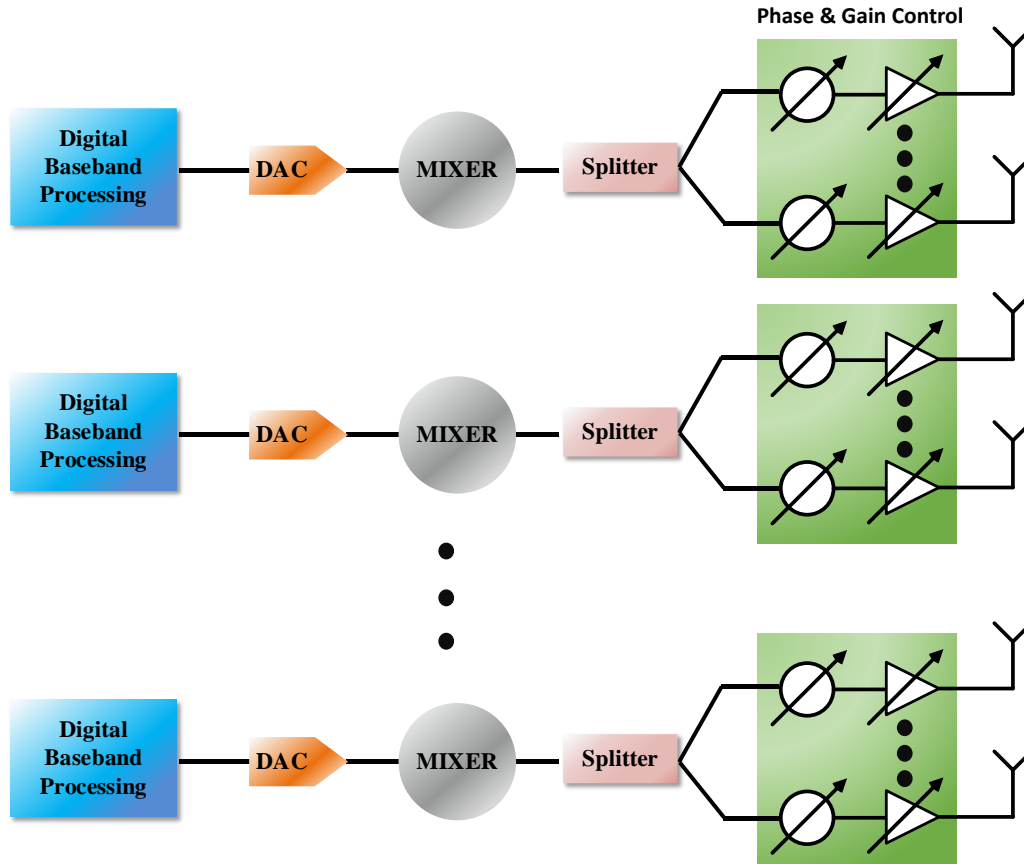


Figure 2.5: Hybrid Beamforming Architecture

It should be noted that equation 2.2 satisfies to any 2D phased array, even the one with irregular element positioning.

Based on different architectures, beamforming techniques can be categorized into three major types: RF (Analog), digital and hybrid. In RF beamforming, the whole phased array only has one digital signal processor. After that digital signal is converted to analog signal through digital-to-analog converter (DAC) and upconverted to higher frequencies through mixer, it is equally splitted into all antenna elements. The beam is controlled by the phase

shifters in RF domain of each channel, after the power distribution networks (Fig. 2.3). Its relatively simple hardware implementation makes it a cost-effective solution, especially at mm-wave where power and spacing sources are scarce. In digital beamforming, each antenna has dedicated digital baseband signal processing where the phase shift is done. While providing the most precise and flexible beam control, digital beamforming suffers from high power consumption and numerous hardware overheads, because each antenna needs its own mixer and DAC (Fig. 2.4). Lastly, hybrid beamforming (Fig. 2.5), as the name indicated, combines the advantages of RF and digital beamforming and it can be treated as the multiple rf beamforming being put together.

## 2.2 Literature on RF Beamforming Array Construction Below 100 GHz

Rel-16 of 3GPP supports NR operation in FR2 covers the frequency ranges n257-n262, which correspond to 24.25 GHz to 29.5 GHz, 37 GHz to 43.5 GHz and 47.2 GHz to 48.2 GHz [34]. In the recent Rel-17, 3GPP has decided to extend FR2 operation to 52.6 GHz to 71 GHz which offers an abundance of available unlicensed spectrum around the world that was previously only exploited by WiGig [35]. Therefore, recent antenna arrays with their silicon chips have been mainly demonstrated at 28 GHz, 39 GHz and 60 GHz, some other works are Ku-band satellite communication (SATCOM) and W-band frequency-modulated continuous wave (FMCW) automotive radars, as shown in Fig. 2.6 that exclusively includes works that integrate antenna and beamformer chips altogether. There are three main approaches for the construction of beamforming antenna arrays, i) Antenna-on-PCB, ii) Antenna-in-Package and iii) Antenna-on-Chip.

### 2.2.1 Antenna-on-PCB

This method embeds antenna structure into PCB, then pre-packaged BFICs are typically wire-bonded or flip-chip mounted on the opposite PCB side to array if antenna is implemented in planar structure, or lateral to array if antenna is end-fire.

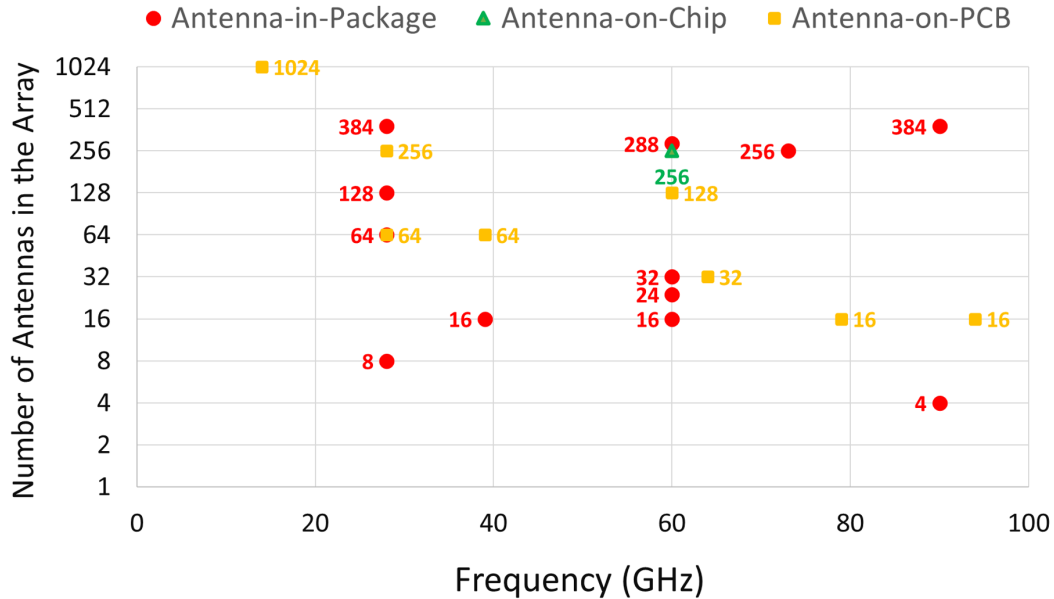


Figure 2.6: A survey of phased array construction choices below 100 GHz [3, 4, 5, 6, 7, 8, 9, 10, 11, 12, 13, 14, 15, 16, 17, 18, 19, 20, 21, 22, 23, 24]

It is prevalent to use multiple quad-channel beamforming integrated chips (BFICs), each chip contains four RF transceiver (TRx) channels, to sum together to form phased-arrays with larger dimensions. Fig. 2.7 shows the block diagram and PCB stackup of such 64-antenna-element phased array from UCSD [15], where a 1:16 Wilkinson power divider/combiner on layer M1 combined with 1:4 on-chip Wilkinson networks, thus a completed 1:64 Wilkinson network with a common RF port is realized. For each coaxial-fed stacked square patch antenna element, the radiation and parasitic patches are designed on M10 and M12, respectively, to improve the antenna operating bandwidth by creating two resonances. Layer M6 serves as antenna ground, while layers M7 to M9, and M11 contain no metal to maintain the overall stackup symmetry and the optimized antenna performance concurrently. Such implementation achieves 22.64% frequency bandwidth centered at 26.5 GHz. Because the gain of a phased array is proportional to its physical aperture size thus number of elements, it is desired to design phased array as module that can be

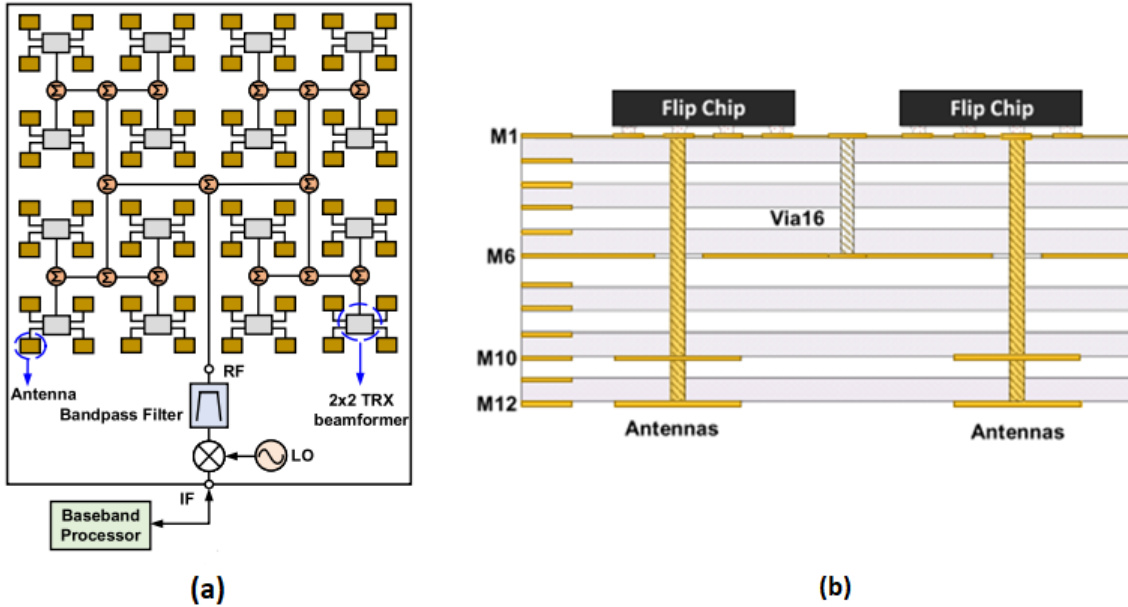


Figure 2.7: (a) Block diagram of the wideband 5G 8×8 phased array. (b) Stackup of low-cost 12-layer PCB. [15]

easily expanded to larger dimensions without adding too much extra design complexity. A valid solution is introduced and displayed in Fig. 2.8, with the same aforementioned stack up and antenna structure, a 256-element dual-polarized subarray is first designed at 14 GHz, 1024-element phased array is built by four identical subarray quadrants after [13]. But here besides 64 quad-channel BFICs for 256 antenna elements, an additional BFIC is placed at the subarray centre works as a driver to calibrate the residual error between each quadrant. Overall, the array achieves an impressive effective isotropic radiated power (EIRP) of 75 dBm and very wide scan angles of  $\pm 75^\circ$  in both planes. Another example is presented in Fig. 2.9 from the Tokyo Institute of Technology, each module has 4 quad-core BFICs with 24 circular-shaped patch antenna (includes 8 dummy elements to improve the performance of edge elements on E-plane) centered at 39 GHz [17]. Four modules are assembled side-by-side to form a 64-element phased array.

However, this approach requires the size of quad-channel BFICs to be inversely pro-

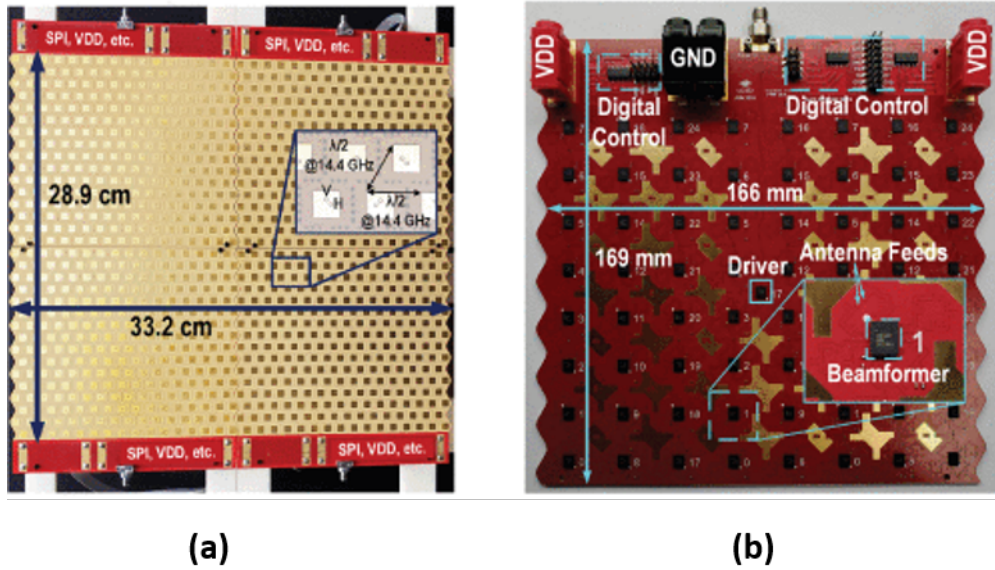


Figure 2.8: (a) Antenna side of 1024-element Ku-band SATCOM TX array. (b) Chip side of 256-element Ku-band SATCOM TX quadrant. [13]

portional to the antenna center frequency. At higher frequencies, the BFICs need to be miniaturized to maintain the optimal antenna element spacing of  $\lambda/2$  both within and between each 2x2 subarray which is not always feasible. Take the example as shown in Fig. 2.10, the element spacing on vertical plane increases to 3.5 mm ( $0.7\lambda$  @60 GHz) for the accommodation of BFICs, RF transmission lines and digital routing [14]. Since at 60 GHz,  $0.5 \lambda$  is 2.5 mm, but the size of quad-core BFICs are  $2.5 \times 3.3 \text{ mm}^2$  which are not able to leave sufficient vertical spacing between the elements. As a result, the scan range on E-plane is limited to only  $\pm 15^\circ$ .

## 2.2.2 Antenna-in-Package

The idea of this approach is to divide the system into two levels, the first level is similar to antenna-on-PCB which implements antennas directly on PCB with flip-chip bonded BFICs on the opposite side of array. But, usually each chip has relatively larger number of channels (16-32). Next, the first level package tiles with embedded antenna can be

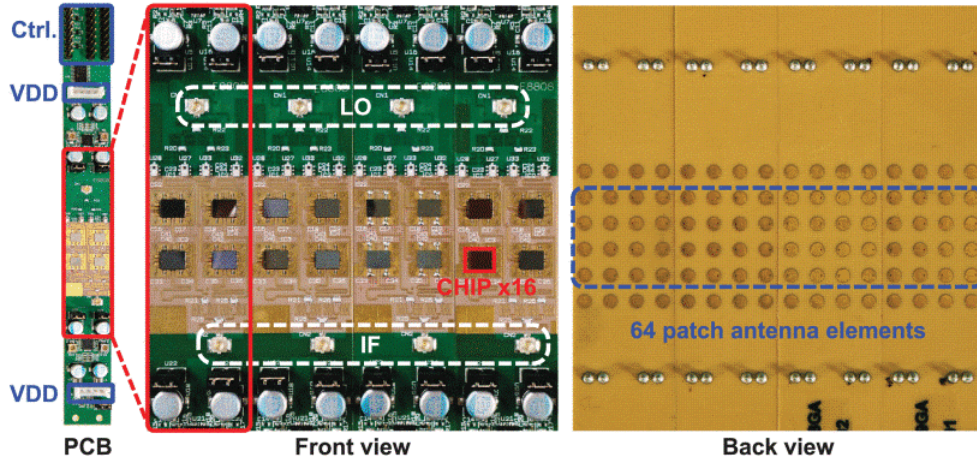


Figure 2.9: Implemented PCB with patch antenna on the back side [17]

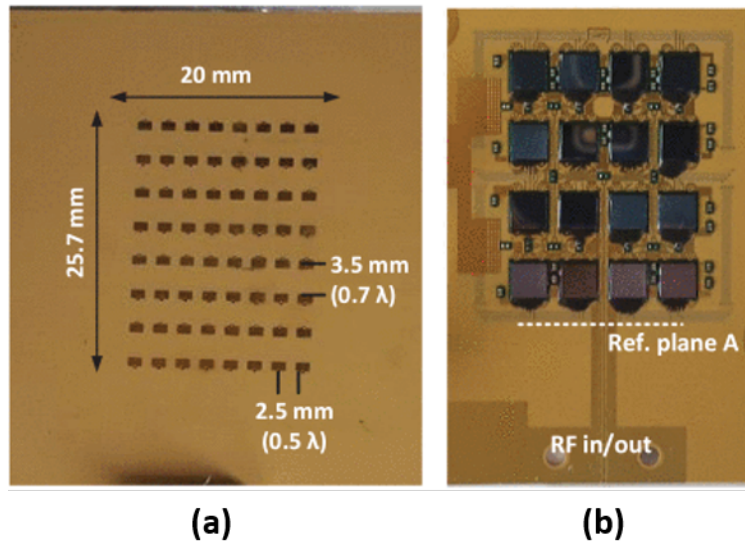


Figure 2.10: (a) Antenna view. (b) Chip view and  $8 \times 16$  phased-array. [14]

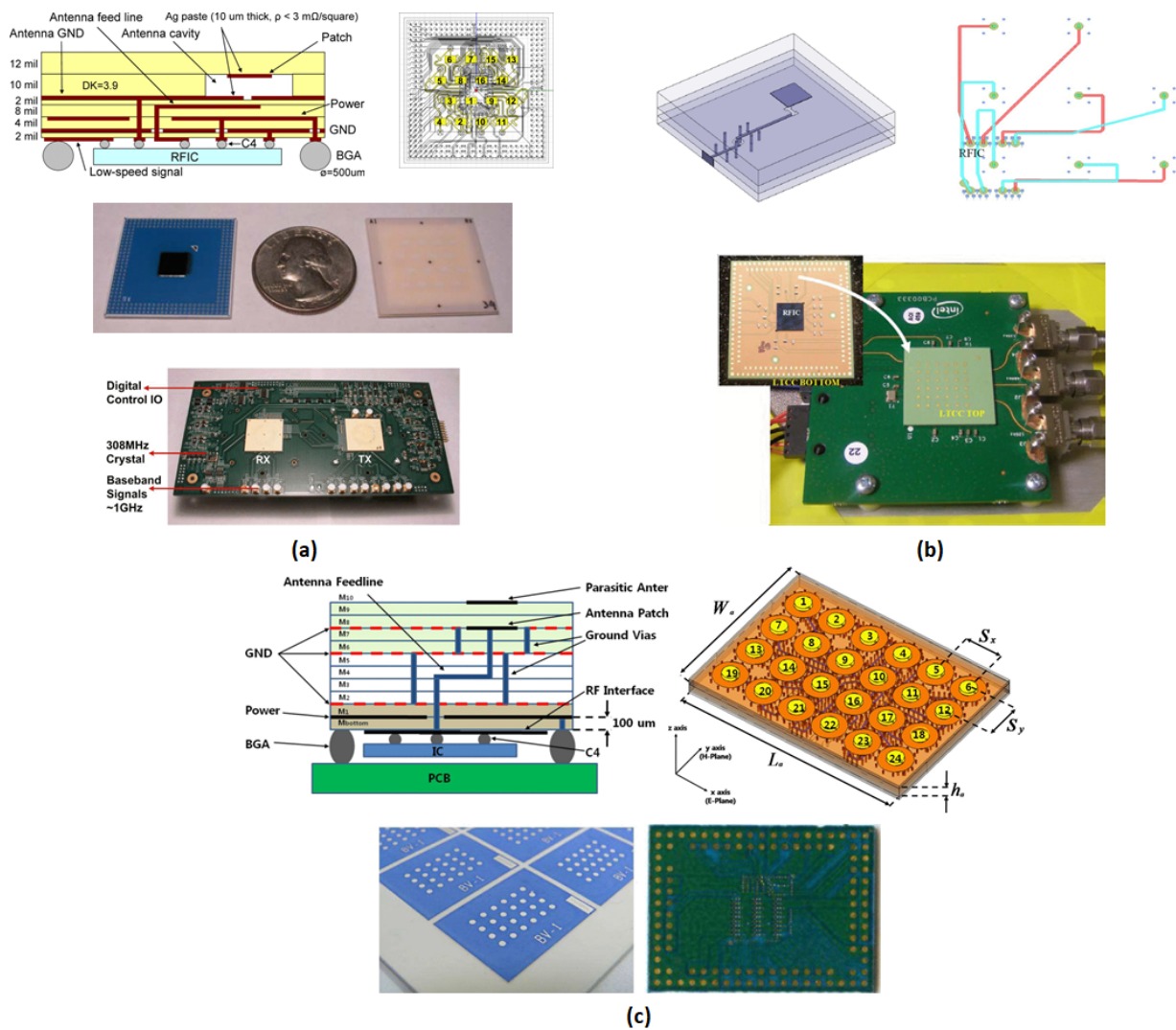
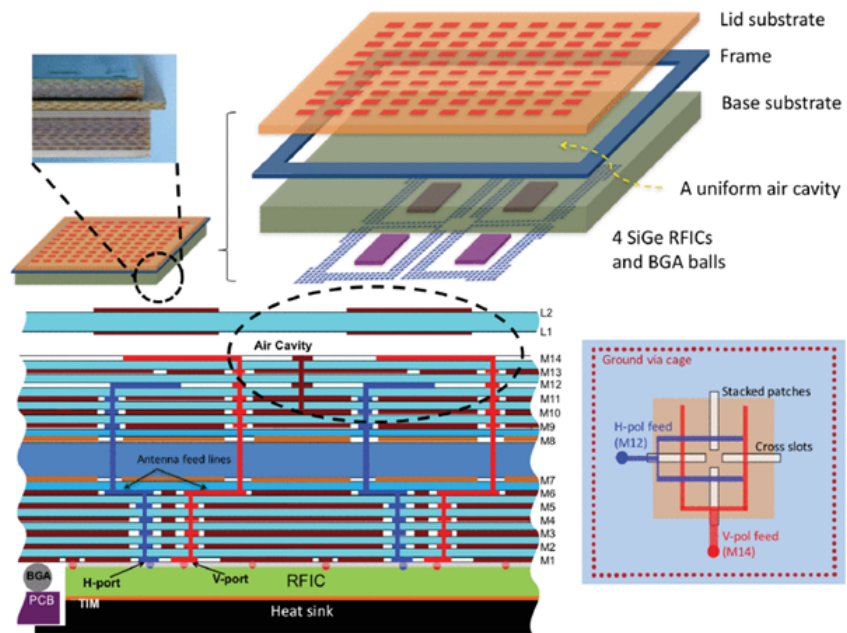


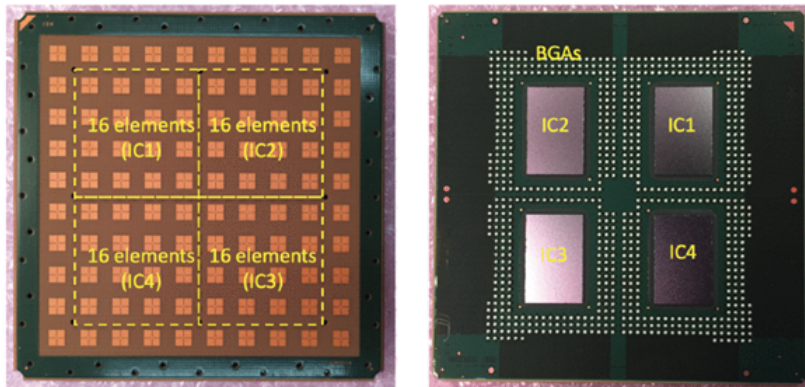
Figure 2.11: Demonstrated Antenna-in-Package with LTCC substrate from (a) IBM [25], [26] (b) Intel [7] (c) Samsung [23]

assembled on the second level low-cost PCB that has bulky digital/DC through ball-grid arrays (BGAs).

In the early 2010s, as summarized in Fig. 2.11, several companies facilitated multi-layer Low-temperature co-fired ceramic (LTCC) as substrates in their 60-GHz antenna-in-



(a)



(b)

Figure 2.12: (a) Illustration of the antenna-in-package assembly breakout, layer stack-up, antenna feeds, and board-level mounting concept. (b) Top view and bottom view of a fully assembled antenna array package with mounted BGA solder balls and four transceiver ICs. [19]

package demonstrations because of its capability of 3D design such as cavities, and high thermal conductivity. In [25], [26], aperture-coupled patch antenna is design in LTCC package which includes air cavity between radiation patch and antenna ground to enhance the bandwidth and efficiency. The transmitter (Tx) and receiver (Rx) ICs are then flip-chipped to the packages and connect to the patch antennas through microstrip transmission lines and transition vias. Each IC supports sixteen antennas and the whole 28mm x 28mm 288-pin BGA packages is lastly assembled on a evaluation boards which contains digital control IO and some other bulky surface-mounted passive components. This array achieves 9 GHz bandwidth centred at 60 GHz and 5 dBi unit antenna gain across the operating bandwidth. Intel [7] also presented a 32-element symmetrical Tx/Rx 60-GHz BFIC mounted on LTCC which integrates 6x6 patch antennas includes four dummies to achieve 19 dBi gain with scanning of  $\pm 30^\circ$ . In [23], the key differences between prototype and product level design are discussed, nonstandard fabrication techniques and high manufacture cost are two major barriers for commercialization of antenna-in-package.

Hence, accompany with thriving and prosperous of advanced PCB process (e.g. Hybrid PCB), organic substrates becomes a more attractive package solution. Illustrated in Fig. 2.12, IBM [19] reported 64-element dual-polarized 28-GHz phased-array antenna module which the package comprises a two-layer lid that has stacked antenna patch on it, a two-layer frame to create air-cavity, and a 14-layer organic base substrate. Unlike previously introduced single-IC implementation, each package has 64 active elements fed by four ICs and 36 dummies placed at the edge. Fig. 2.13 shows an alternative of realizing antenna-in-package with larger dimension from Qualcomm. In this work, sixteen modules, each integrates two ICs and 16 active dual-polarized antenna elements, are tiled on a PCB to form a 256-element antenna array. Each module is fed by two RF common ports through Wilkinson combining network on PCB. It is clearly seen that the RF feeding network and PCB stackup can be significantly more complicated than those use antenna-on-PCB approach, especially in the dual-polarized cases.

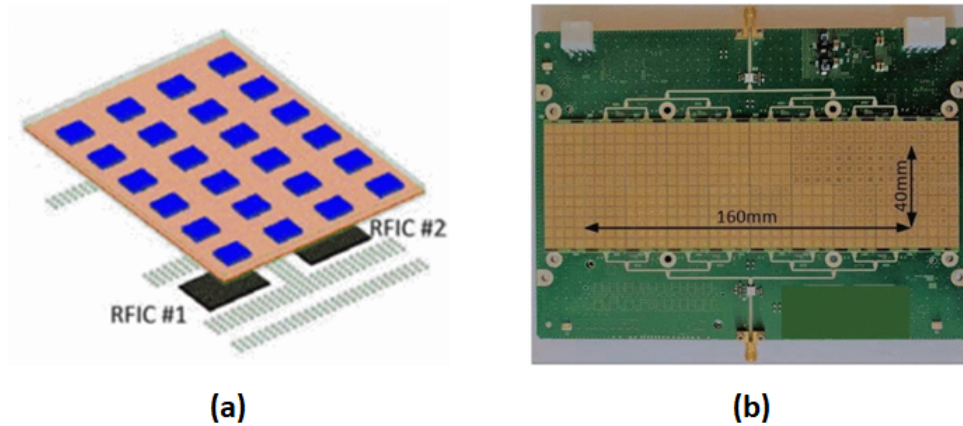
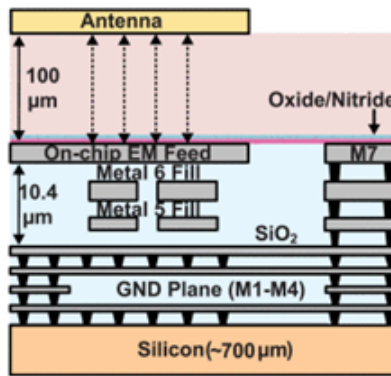


Figure 2.13: (a) Base station antenna tile with 4x4 active patch array and 2x4 dummies [20]. (b) Gnb prototype photo [21].

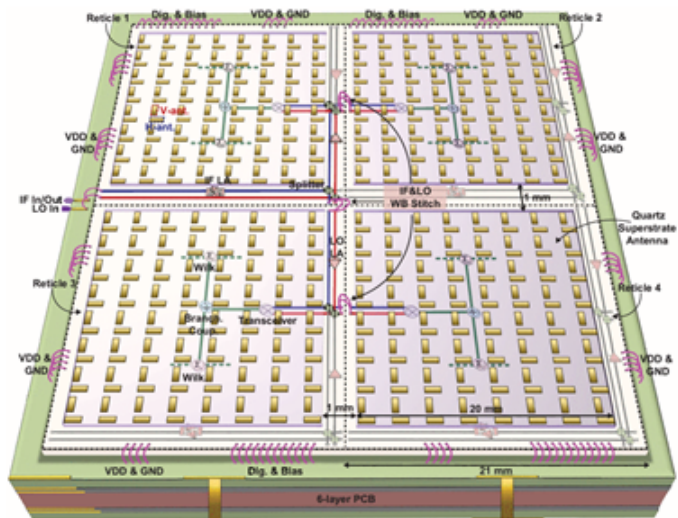
### 2.2.3 Antenna-on-Chip

To further increase the integration level and minimize the transition loss from BFICs to the antenna, the idea of antenna-on-chip is to implement antenna elements directly on BFICs, which is also known as wafer-scale phased-array approach. At low-frequency applications, the antenna size is much larger than the chip size which impedes the realization of on-chip antenna. However, with the unprecedented growing demand of higher data rate and larger bandwidth over the past decade, the use of mm-wave and sub-terahertz frequency bands pushes the miniaturization of antenna arrays and open the door to such solution.

Despite the advantages of achieving the highest integration level by putting almost all the blocks of Tx/Rx chain in one chip and the better Signal-to-Noise ratio (SNR) by avoiding the long transmission line for RF path transition, low radiation efficiency is the most critical drawback of antenna-on-chip applications. A common substrate used in silicon based CMOS stackup has a low resistivity of about  $10 \Omega\text{-cm}$ . This electrical property of semiconducting substrates help ICs to alleviate latch-up but seriously deteriorate the antenna performance. Instead of being radiated to the air, the electromagnetic wave chooses the path with lower-resistivity through the substrates and dissipated as heat. In addition, high dielectric constant of silicon suppresses more RF power in the substrates and gen-



(a)



(b)



(c)

Figure 2.14: (a) Cross section of high-efficiency differential dipole antenna. (b) Block diagram and photo of bondwire-stitched 256-element phased array board. [12]

erates surface waves which distort the desired antenna radiation pattern. Unfortunately, some of the conventional efficiency enhancement approaches such as selectively etching an air cavity under the area of antenna patches becomes no longer easy to apply, it requires nano-fabrication processes that pose manufacture complexity and difficulty. Several early investigations of on-chip antennas reported radiation efficiency of only 10-15% [36], [37].

More recently, implementations of superstrate layers have been reported for improving radiation efficiency of on-chip antenna, a representative piece of work is illustrated in Fig. 2.14a. A 100- $\mu\text{m}$ -thick quartz superstrate ( $\epsilon_r = 3.8$ ) is attached on the wafer to act as a quarter-wavelength impedance transformer between Silicon dioxide and air. Antenna element is implemented on top of quartz layer, the ground plane and EM-coupled differential microstrip feed are on the M4 and M7 layer, respectively. Two separate antenna elements are placed orthogonally for dual-polarization. The quartz antenna efficiency can be further improved to over 70% by using two quartz layer at 60 GHz, however, it causes the assembly tolerance issue and offset has to be well-controlled. It is also worth mentioning that, by employing redundant interfaces and reticle-to-reticle stitching technique, four 2 x 64-element phased array quadrants successfully form a 2 x 256-element phased-array (Fig. 2.14b).

## 2.2.4 Comparison

After surveying three principle topologies of phased array construction, it is instructive to compare different perspectives of these approaches to have a comprehensive view of their feasibility. Table. 2.1 comparatively summarizes critical attributes of each method.

- **Suitable Frequency:** Due to the inversely proportional relationship between per IC area and antenna operating frequencies, most of the works that implement 2x2 BFICs with PCB-based antenna are designed at  $< 60$  GHz. The design rule of conventional PCB forbid fine structures in traces width, via size and IC package bump. There are several exceptions above 60 GHz that implement BFICs with large number of channel and place the chips laterally to the antenna element, but those are designed for only 1-D array. Because of the flexibility of two-layer packaging and large number

Table 2.1: Comparison of various approaches of phased array construction.

	Antenna-on-PCB	Antenna-in-Package	Antenna-on-Chip
Suitable Frequency	< 60 GHz	20-100 GHz	> 100 GHz
Antenna Efficiency	High	High	Low
Transition Loss	High	Medium	Low
Integration Level	Low	Medium	High
Design Complexity	Low	Medium	High
Array Scalability	Easy	Easy	Hard
Manufacture Cost	Low	Medium	High

of channels per chip, antenna-in-package is suitable for the frequency bands spread in the range of 20-100 GHz. As for antenna-on-chip, the work demonstrated below 100 GHz is nearly scarce mainly due to considerable antenna element size at lower frequencies.

- **Antenna Efficiency:** Because of the low resistivity of silicon substrate, on-chip antenna suffers from low efficiency, while both antenna-on-PCB and antenna-in-package can achieve above 90% of efficiency by using dielectric materials with low loss tangent ( $\tan \delta$ ).
- **Transition Loss & Integration Loss:** There is no doubt that antenna-on-chip method has the highest integration level because it theoretically eliminates the transition loss from the chip to antenna. However, whether antenna-on-pcb or antenna-in-package has lower transition loss remains debatable and needs to be assessed case by case. Compare to antenna-in-package with larger number of channels in each BFIC, 2x2 Quad IC approach in antenna-on-PCB has relatively shorter equal-length connections from ICs to antennas but requires more stages of power distribution network.
- **Design Complexity:** Wafer scale antenna has the highest design complexity among three construction methods, because co-design of beamformer circuits and antennas

is a necessity for optimal performance which is largely dedicated by foundry-defined layout rules. When designing antenna-in-package, all solder-based bump interfaces that interconnect between BFICs, the first-level package and the second-layer bottom PCB need to be fine modeled and characterized to minimize the risk of assembly failure, thereby requires additional design effort in contrast to antenna-on-pcb.

- **Array Scalability:** Both antenna-on-pcb and antenna-in-package implement multiple number of BFICs to form beamforming array, each BFIC has identical feeding network to antennas so that the array can be expanded to larger size while preserving symmetry. Antenna-on-chip has to apply stitching technique and reserve redundant digital control pin to enable scalability which pose considerable difficulty to achieve.
- **Manufacture Cost:** The most renowned advantage of directly implementing antennas on PCB is its lower manufacture and assembly cost than the other two methods, because Antenna-in-package requires additional package process and each IC has large I/O count, and Antenna-on-chip requires stitching technique and quartz superstrate, as both of them remarkably increase the costs.

## 2.3 Literature on Transmitter Observation Receiver

Although the capability of RF beamforming arrays to generate high EIRP and fast beam switching in the user direction with limited digital signal processing resources has been extensively proved to be an future-enabler for 5G NR, there are still two major challenges to be addressed.

1. 5G employs high-order modulations and OFDM signal for wireless communications which requires rigorous linearity in order to achieve low error vector magnitude (EVM) and high adjacent channel power ratio (ACPR). However, power amplifiers are non-linear by nature and introduce spectral regrowth. DPD has so far been widely adopted to improve the linearity.
2. Ideally, in RF beamforming array setup, a single common RF input is splitted equally into multiple transmitter channels and expected to have same response. In reality,

not only the unavoidable manufacture tolerance causes channel-to-channel or chip-to-chip variation, but also phase and amplitude of each channel vary over time because of aging or deploy environment change. Therefore, amplitude and phase calibration of each channel have to be performed regularly.

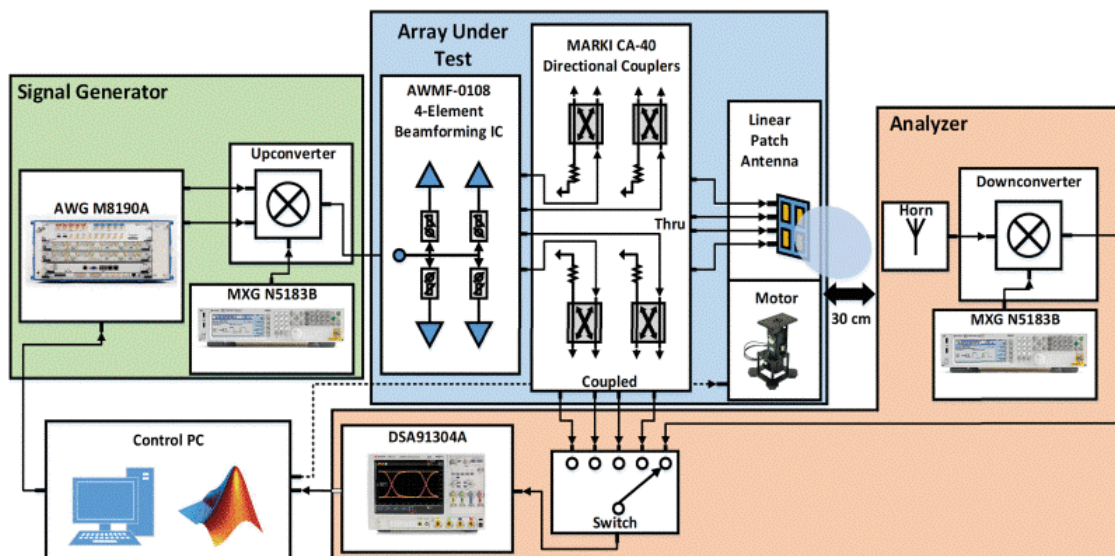


Figure 2.15: Functional block diagram of the four-element array with switch between the output from the receiving over-the-air (OTA) horn antenna and each of the coupled PA lines [27]

Both DPD and array calibration call for a feedback path to acquire the sampled output of each transceiver channel, thus reveal aforementioned challenges. Several studies to implement feedback path in beamforming array have been reported in literature.

The two most intuitive array feedback architectures are conductive [38], [39] and OTA [40], [41], [42]. To provide further flexibility, switchable feedback architectures [43], [44], [27] are also proposed to receive the sampled power amplifier output in each channel and radiated response through FF receiver antenna, one of the examples is displayed in Fig 2.15. However, if there are large number of transmitter channels, inserting couplers to the output of each PA and adding switches can be very cumbersome, then become no longer realistic solutions.

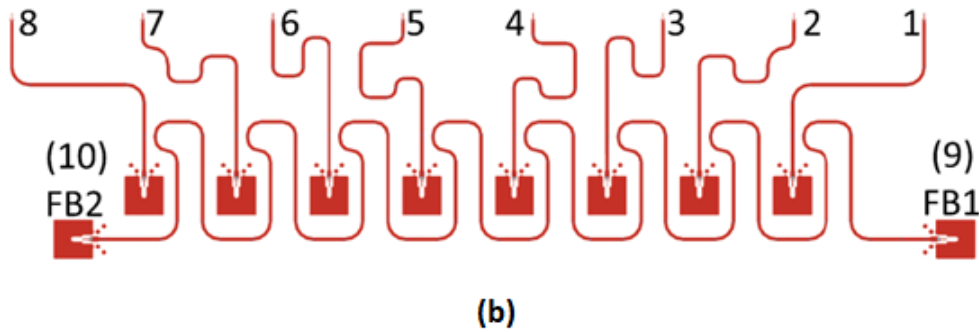
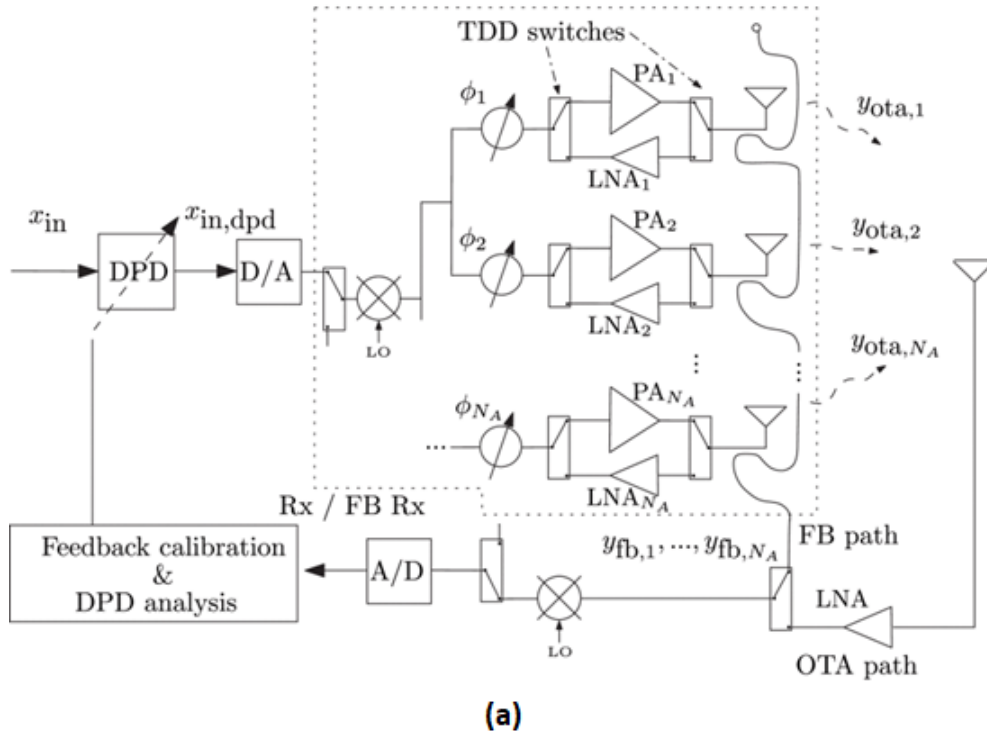


Figure 2.16: (a) Phased-array Tx with DPD using the proposed combined feedback architecture and OTA calibration. (b) Layout picture of the common FB line for eight transmit paths. [28]

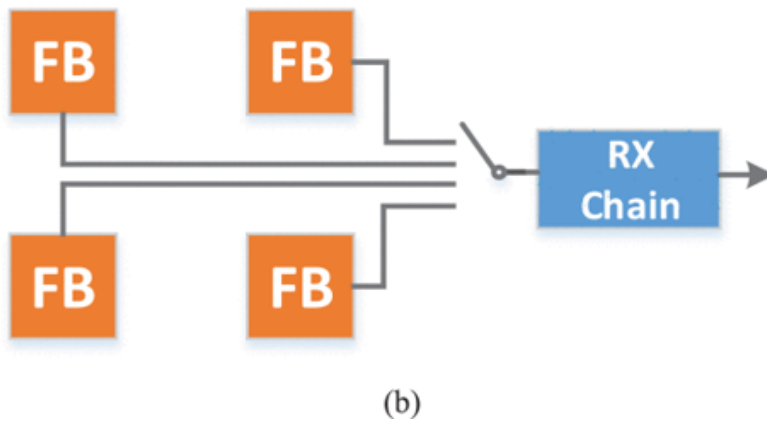
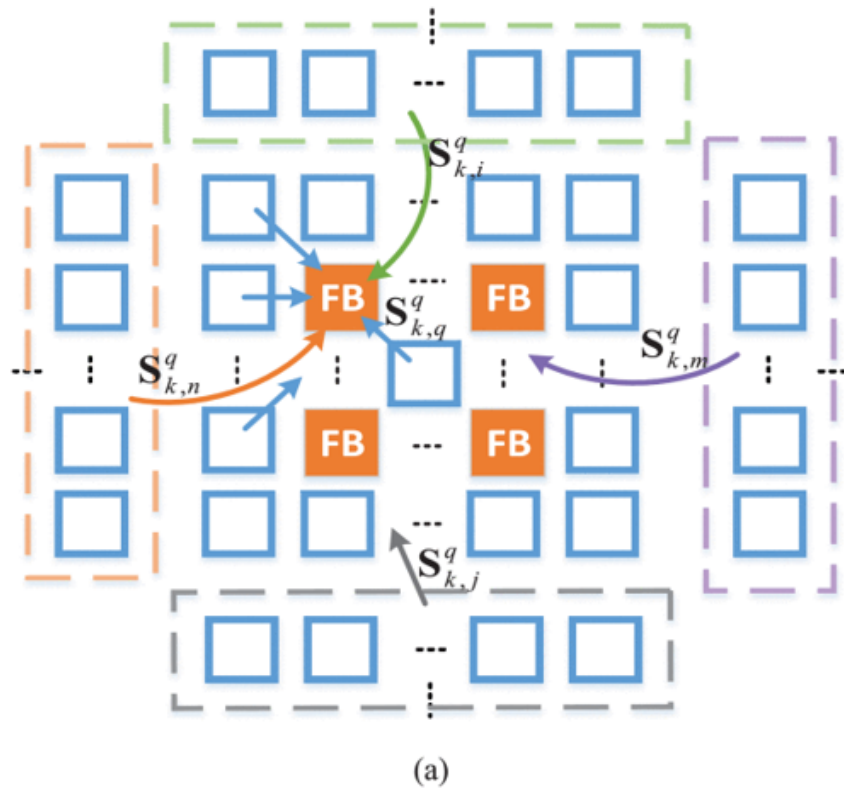


Figure 2.17: Diagrams of over-the-air diversity feedback receivers configuration. (a) Symmetrical diversity feedback receivers configuration. (b) Shared feedback loop. [29]

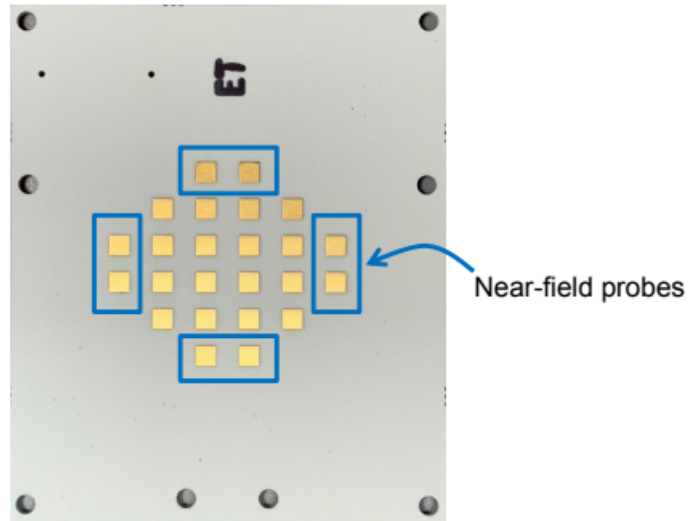


Figure 2.18: 16-element RF beamforming array with near-field probe receivers placed on array perimeters [30]

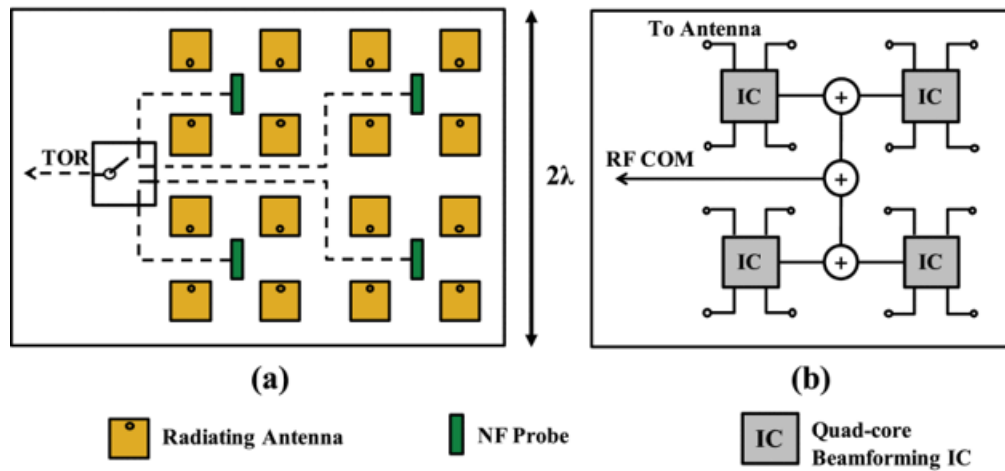


Figure 2.19: Layout illustration of (a) proposed beamforming transmitter with NFPA placed at the center of each 2x2 subarray and (b) four quad-core BFICs (on one module) that feed 16 patch antennas. [31]

As an original idea proposed in [45], in-field calibration and DPD have attracted the attention of many researchers. The authors in [28] proposed to layout a meandering microstrip line between antenna element as shared feedback line that couples all transmit paths as illustrated in Fig 2.16. Combined with the time-division-duplex (TDD) TRx architecture, they are able to active single PA at a time for DPD training and array calibration without adding extra couplers and switches. However, transmission line occupies considerable extra spaces and may force the antenna spacing to compromise which hinders the compatibility of this solution at higher frequencies. In [29], the authors proposed to embed feedback receivers into transmitter phased array and collect the transmitted signal by near-field coupling, as described in Fig 2.17. They validated the principle in both 1x4 RF and 2x3 hybrid beamforming array at 3.5 GHz, with monopole antenna element, which would not be practical for planar arrays, unfortunately. In another attempt to perform DPD training using near-field receivers, [30] suggested placing receiver antenna at the outer perimeter of transmitter phased array as feedback path by utilizing mutual coupling, which is named NFPs, as depicted in Fig 2.18. Through the measurements, cancellation of non-linearity effects in the FF can be achieved if the difference between a properly synthesized near-field target signal and the acquired near-field signal is minimized by DPD training. However, the placement of NFPs at the perimeter of phased array impedes the scalability of it from expanding to larger number of elements which limits the compatibility of this approach. To alleviate this issue, a phased array with uniformly distributed NFPs at 28 GHz is introduced in [31], [46]. As shown in Fig 2.19, for the purpose of sampling wide-band real-world 5G modulated signal to DPD and perform array calibration, the designed NFPs couple to the surrounding four antenna elements with flat coupling magnitude and linear phase response versus frequency. When feeding the array with 400-MHz OFDM modulated signals, excellent phase and magnitude errors of  $2.8^\circ$  and 0.27 dB, respectively, were achieved through in-field calibration by near-field probe coupled data. Additionally, with the same maximum allowed EVM of 3.5%, the NFP based DPD improved EIRP from 27.5 to 33 dBm. This efficient method completely eliminates the need of impractical FF receiver antenna as feedback path for DPD training and enabled the possibility to expand the array to larger size. However, due to the pcb manufacture limitation, BFICs were assembled on the separate adaptor board from the primary antenna board which increased

overall yield. Another drawback is the designed NFPs only worked for single-polarized phased array which does not maximize the use of channel capacity.

## 2.4 Discussion

After introducing the background theory and reviewing different beamforming phased array construction and TOR integration methods, a few conclusions can be made as below:

- Compared to the other two methods (Antenna-in-package & Antenna-on-chip), antenna-on-pcb has non-negligible transition loss and non-optimal integration level, but its affordable manufacture cost, high antenna efficiency and good array scalability has made it a more attractive choice below 60 GHz in literature.
- To design beamforming radio systems in 5G, array calibration and DPD techniques are the key features to enhance the overall Tx performance. Both techniques require a TOR as feedback path to monitor or sample the TX output and synthesize the appropriate calibration and DPD function coefficients.
- The recent state-of-art suggest to utilize mutual coupling and built-in feedback path for DPD and array calibration. However, integrating observation receiver into the same board of Tx antenna causes space-consuming problem and deteriorate the array scan range and scalability. An elegant arrangement of uniformly distributed embedded NFPs was proposed, but it does not maximize the channel capacity.

Based on above discussions, one research topic becomes evident: dual-polarized beamforming phased array with embedded NFPs for 5G wireless communications.

# Chapter 3

## 37-40 GHz 16-Element Dual-Polarized RF Beamforming Phased Array Design

### 3.1 Project Scope

For the purpose of risk management and cost control, it was decided to use RF beamforming and antenna-on-pcb as beamforming phased array architecture in this project, as they are relatively easy to implement while providing good performance. In addition, based on accordingly discussion in the previous chapter, the innovation involved in this project should be embedded NFPs designed for dual-polarized beamforming phased array that has capability of array calibration and DPD.

The design of this project is around the off-the-shelf BFIC from Anokiwave, AWMF-0159, which is a highly-integrated silicon quad-core IC with dual-polarization capability that operates from 37 to 40 GHz. Each IC has two common inputs connected to eight output ports through two in-chip Wilkinson divider such that each IC can support four dual-polarized antennas. Each channel has individual amplitude and phase control. In this chapter, the design of unit cell antenna element and embedded NFPs within RF

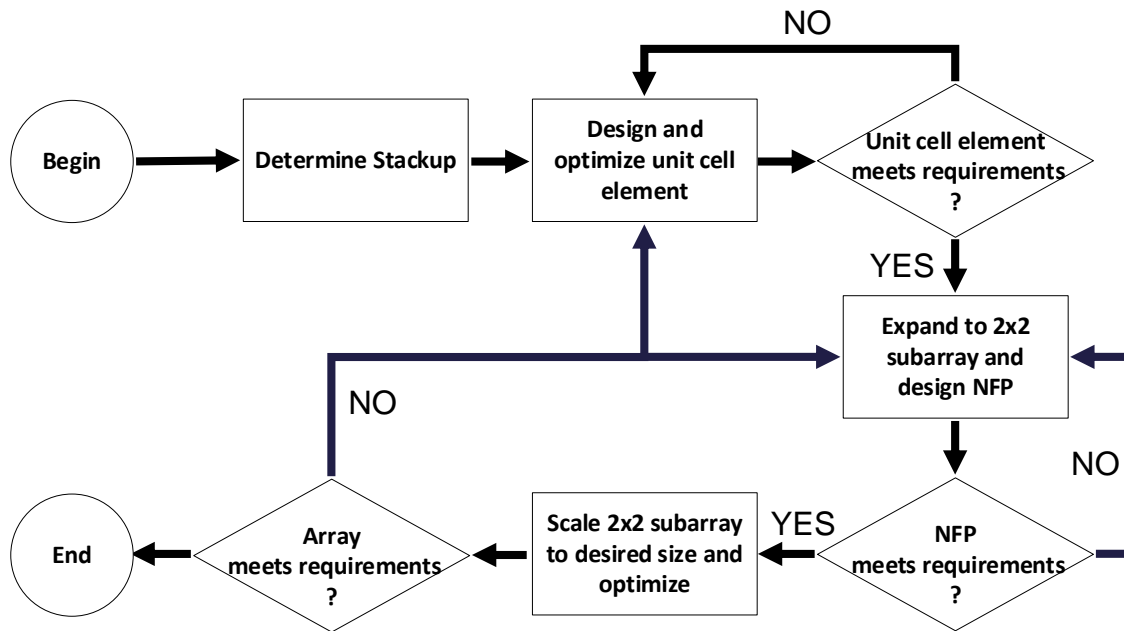


Figure 3.1: Design process of proposed beamforming phased array with embedded near-field probes

beamforming phased array are presented. The general design process is illustrated in Fig. 3.1.

## 3.2 Antenna Design

Despite tremendous advances in utilizing antenna-on-pcb technique in phased array system, designing antennas on PCB at mm-wave continues to face constraints and challenges due to its compact size and restrict manufacture tolerance.

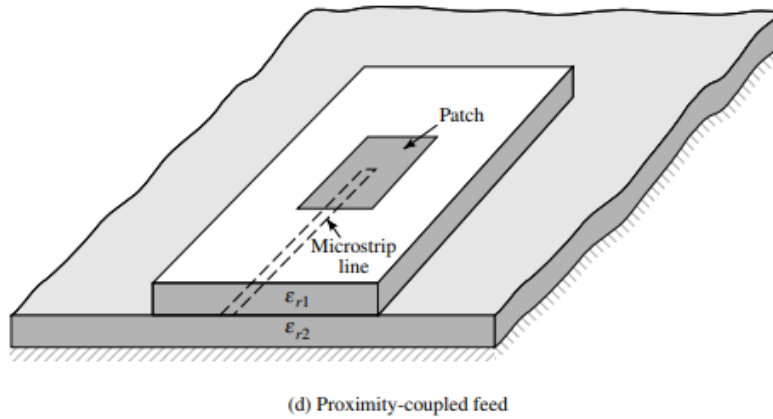
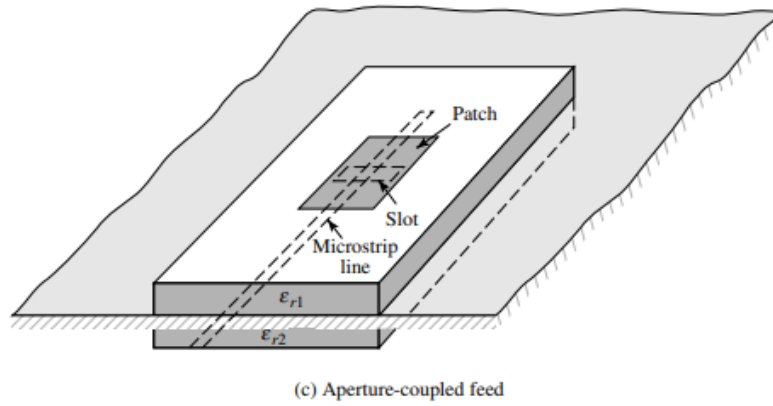
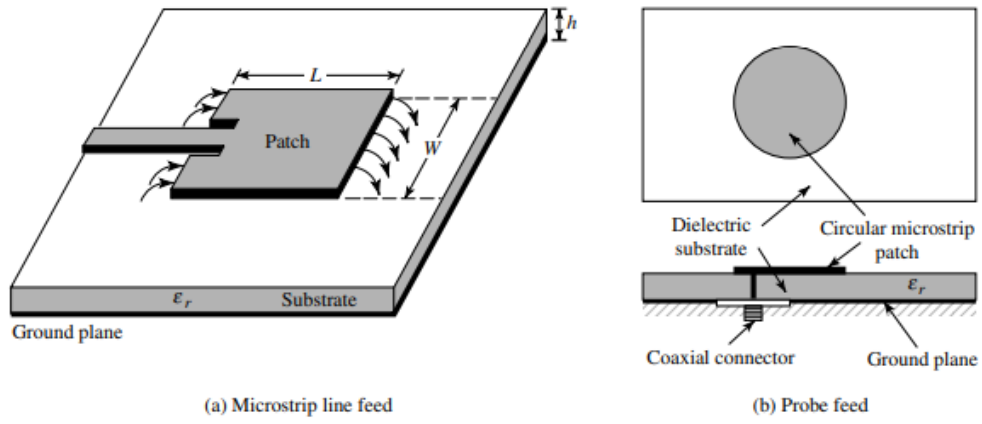


Figure 3.2: Typical Feeds for patch antennas [32]

### 3.2.1 Feeding Mechanism

Patch antenna, also known as microstrip antenna, is built on a thin dielectric plate, with a metal layer attached on one side as ground plate, and the second metal layer on the other side can be made into any desired shape by etching. Its low-profile, broadside radiation, planar surfaces, high design flexibility and low manufacture cost have made it a prevalent solution in phased array design. However, it should be noted that the feeding mechanism has large impact on the antenna overall performance, in terms of bandwidth, efficiency and design complexity.

The most straightforward method is microstrip line feed. As shown in Fig. 3.2a, a narrower microstrip line is connected directly to one edge of the radiation patch. By adjusting the conducting point and dimension of main patch, it is easy to model the antenna to achieve good matching. However, the limited bandwidth (2-5 %) due to surface waves and spurious feed radiation makes it inappropriate in mm-wave array design.

From the cross-sectional view of Fig. 3.2b, coaxial-line feed has inner conductor that is connected to the top patch, and the outer conductor is connected to the bottom ground plane. This method is widely used in phased array design because it has low spurious radiation. In addition, bandwidth enhancement technique such as adding a parasitic patch on top of radiation patch, can be easily implemented without much additional design effort.

To further increase the bandwidth and alleviate the issue of high cross-polarized radiation which is caused by asymmetrical structure of microstrip feed and coaxial feed patch antenna, non-contacting feed methods have been introduced. As displayed in Fig. 3.2c, compared to conventional microstrip line feed, aperture-coupled feed has a ground plane separates bottom microstrip line and top radiation patch. The signal is EM-coupled through the slot at the ground plane then to the top patch. Good polarization purity can be achieved by designing the slot at the centre below the patch.

Lastly, as shown in Fig. 3.2d, proximity-coupled feed provides the widest the bandwidth of four methods (15%). In addition, it requires one less metal layer than aperture-coupled feed since the microstrip line feed is right underneath the radiation patch. Another advantage of proximity-coupled is that it reduces the routing difficulty, especially at higher frequencies. As illustrated in Fig. 3.3a, the optimal spacing between antenna elements is

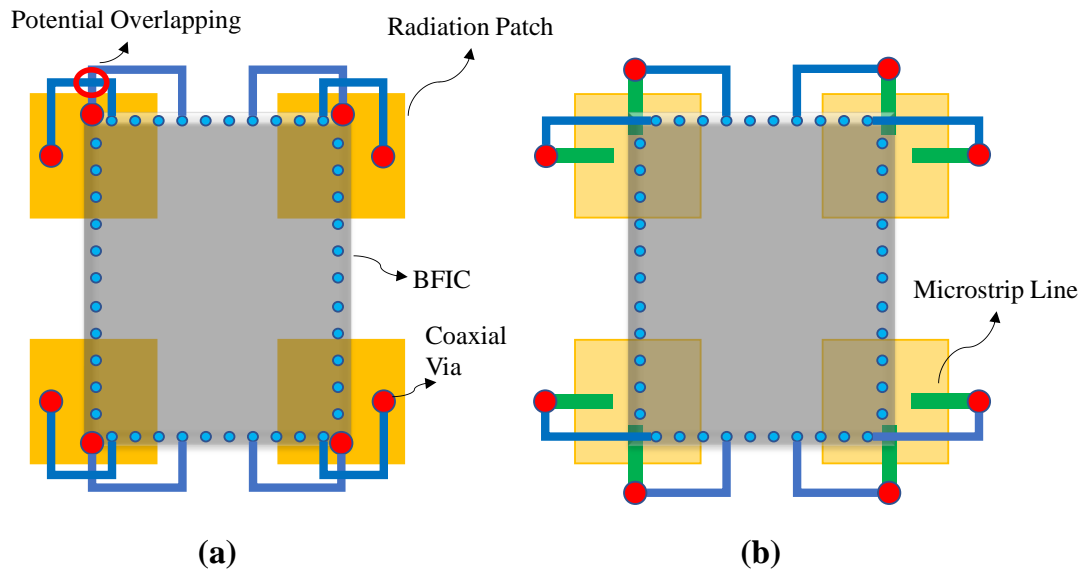


Figure 3.3: Routing of (a) coaxial-feed (b) proximity-coupled feed patch antenna

inversely proportional to the operating frequencies, so the BFIC size is usually comparable to that of  $2 \times 2$  subarray at mm-wave which poses overlapping issue. In order to avoid transmission line overlapping, the designer needs to use multi-layer transition to route one of the RF signal from bottom layer to middle layer which poses more loss and manufacture cost. However, by implementing proximity-coupled feed, the feeding is done through microstrip line located at the metal layer under the patch such that the via transition point can be moved outside of the patch area, as shown in Fig. 3.3b.

### 3.2.2 PCB Stackup

In general, a bare PCB is comprised of metal layers and substrate material. Substrate material can be divided into two different types, core and prepreg. The former one, core, is a solid foundation material coated on both sides with copper. And the latter one, prepreg, essentially can be the same material as core but is impregnated with resin, works as glue to hold cores together. It should be noted that the standard thickness of substrate

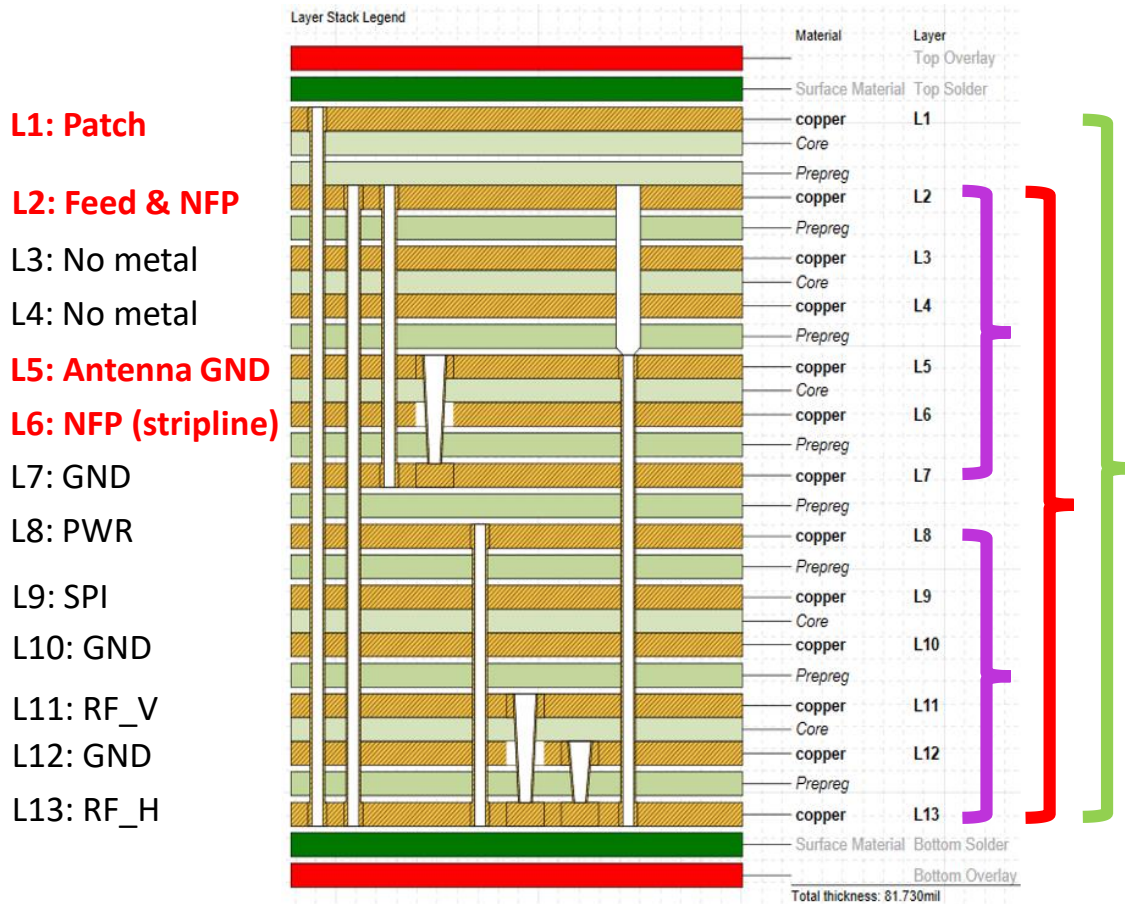


Figure 3.4: PCB stackup and lamination logic used in project

material is usually pre-defined by manufacturers, antenna designer needs to follow that resolution to optimize substrate thickness between radiation patch and antenna ground plane. In addition, the actual thickness of each substrate layer after lamination would change and is dependent on the percentage of copper on the top and bottom metal layer. The estimated thickness can be provided by PCB fab-houses which means a few iterations of optimization might be needed. The lamination logic is given as below: The stackup that was used in this project is illustrated in Fig. 3.4, it consists of 13 metal layers, both prepreg and core are constructed by Isola Astra MT77 with dielectric constant equals to 3.0. It has radiation patch on the top layer, proximity-coupled microstrip feed line and

near field probe at the second layer. As explained in previous subsection, the proximity-coupled fed patch antenna was implemented to enhance the bandwidth and simplify the routing. There is no metal at L3 and L4 underneath the antenna area, it was determined to not only optimize the antenna performance, but also to maintain the symmetry of whole stack up for robustness and cost-saving. By doing so, sub-stack L2-L7 and L8-L13 are identical and can be fabricated in the same lamination cycle. L5 is antenna gnd. The layer beneath is reserved for the transmission line to receive coupled signal from near field probe which will be used for calibration and DPD. Then, the arrangements of rest of the layers are very straightforward, L8 is served as power layer for the 1.8V required by Anokiwave AWMF-0159 BFIC. Lastly, L9 is for serial peripheral interface (SPI) digital control and two Wilkinson networks are at L11 and L13. The overall board thickness is around 80 mil which is 2 mm.

Via is another important aspect of PCB stackup. Since this highly-integrated phased array board requires multiple layers for different RF signals, each needs via to transit signal from bottom layer (where the BFICs are soldered on) to the corresponding layer. In fact, the number of lamination cycle is largely determined by desired via type.

- Lamination cycle 1: First, two identical sub-stack L2-L7 and L8-L13 are manufactured. Afterwards, buried via 2:7 and 8:13 can be done by mechanical drilling. Buried via 5:7, 11:13 and 12:13 can be done from bottom of each sub-stack by controlled-depth laser drilling, which is also named micro-via. It should be noted that the minimum diameter of each type of via is determined by manufacturer aspect ratio (the ratio between the depth of the hole and the diameter of the hole) capability.
- Lamination cycle 2: Sub-stack L2-L7 and L8-L13 are laminated together by prepreg between L7 and L8. Then blind via L2-L13 can be done by mechanical drilling and blind via L5-L13 can be done by back-drilling on blind via L2-L13. Back-drilling is a technique used to remove undesired stub by re-drilling a previously-manufactured through via, with a slightly larger drill.
- Lamination cycle 3: Lastly, L1 is laminated on top of sub-stack L2-L13 to form the complete stackup and through via L1:L13 can be done by mechanical drilling.

The purposes of each different type of via are listed in Table. 3.1.

Table 3.1: Purposes of each type of via in PCB stackup.

Via Type	Purpose
Thru 1:13	Board Assembly
Blind 2:13	Antenna Feed Transition / NFP Receive
Buried 2:7	NFP Transition
Buried 5:7	Shielding GND for NFP Stripline
Blind 5:13	Shielding GND for Antenna Feed Transition
Blind 8:13	Digital / Power Routing
Blind 11:13	Wilkinson Transition
Blind 12:13	GND for BFIC and RF Transmission Line

### 3.2.3 Dual-Polarized Patch Antenna

In 5G wireless communication, it is desired to implement polarization diversity technique on phased array to improve the channel capacity and spectrum efficiency. The two orthogonal feed enables the dual-polarization capability. So that two different signals can be transmitted in two orthogonal planes simultaneously. Unfortunately, this method suffers from poor port-to-port isolation which is an important indicator of signal purity, especially at high frequency because the separation between two ports becomes very close.

The dual-polarized unit cell, from the reference ports at exact position of IC output including coplanar waveguide with ground (CPWG) transmission line at bottom layer and coaxial transition, was simulated in a finite element method (FEM) simulator (HFSS), and the results are presented in Fig. 3.5. In the initial design, two microstrip feed lines are placed right-angled at Layer 2 to proximity-coupled feed to top radiation patch. The input matching of vertical-polarization (V-pol) and horizontal-polarization (H-pol) maintain below -10 dB from 34.2 to 43 GHz, and from 35 to 40.7 GHz, respectively. It is desired

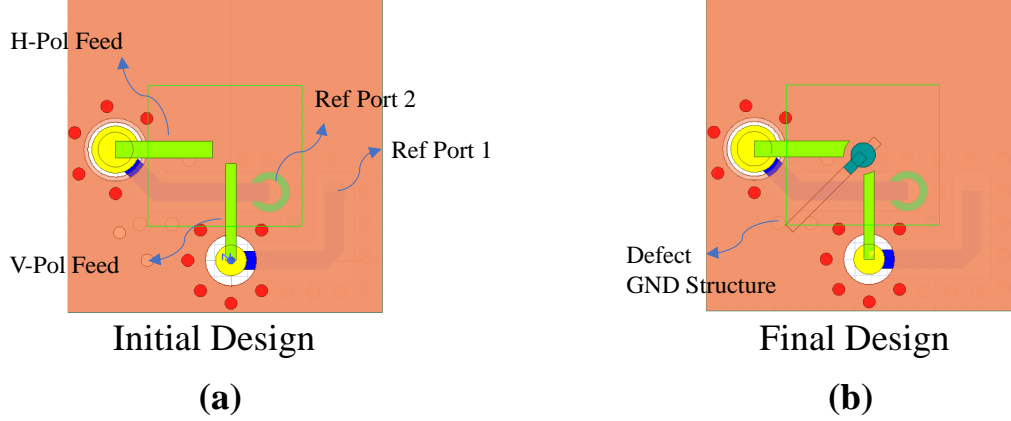
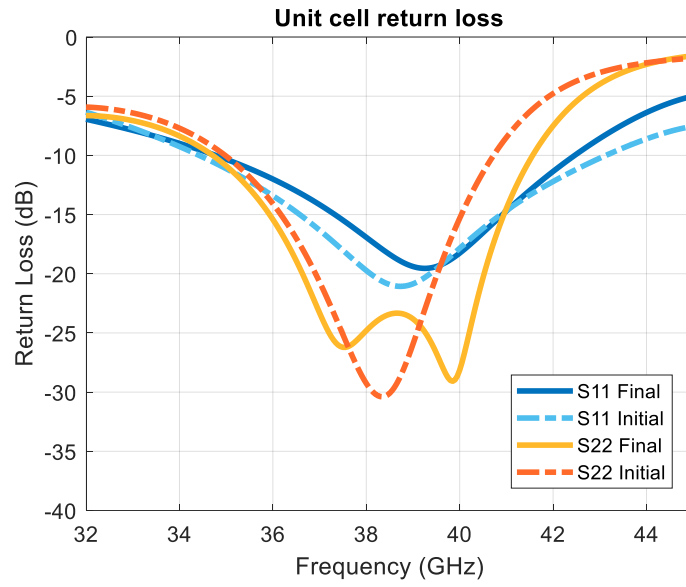


Figure 3.5: Top view of (a) initial design (b) final design of unit cell element

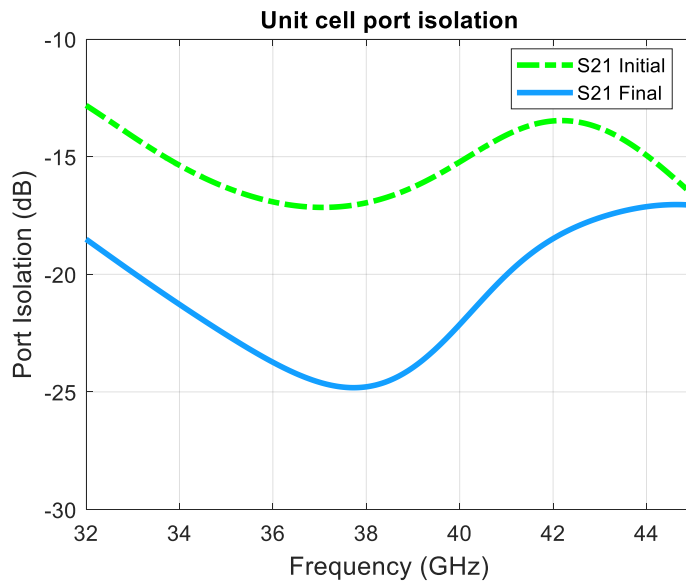
to design antenna at least 2 GHz wider bandwidth than that of BFIC, to allow for 1 GHz frequency shift due to the unavoidable manufacture tolerance. However, the port isolation between two polarization is as high as -15 dB over the operating frequency band. Therefore, a defected ground structure was etched on antenna ground layer (L5) to suppress the surface waves, as illustrate in Fig. 3.6. The -10 dB impedance bandwidth remains the same for V-pol and increases to 35 to 41.7 GHz for H-pol. More importantly, the port isolation improved about 8 dB to as low as -25 dB at 38 GHz.

The design parameters of the dual-polarized proximity-coupled feed patch antenna are illustrated in Fig. 3.7.  $W$  and  $L$  are the physical dimension of the radiation patch at top layer. From cross-sectional view of board,  $h_1$  is the substrate height between the microstrip feed line and top patch, and  $h_2$  is the substrate height between the feed line and antenna ground. For the coaxial via transition,  $d_1$  is the diameter of the feed and  $D$  is the center-to-center distance between feed via and GND shielding via which helps with matching.  $Lh$  and  $Wh$  are the physical dimension of microstrip feed line for H-pol,  $Lv$  and  $Wv$  are the physical dimension of microstrip feed line for V-pol.

Overall, these design parameters were optimized to achieve above-described simulation results. The final value of those parameters after optimization are listed in Table. 3.2.



**(a)**



**(b)**

Figure 3.6: Simulated (a) input matching (b) port isolation versus frequency

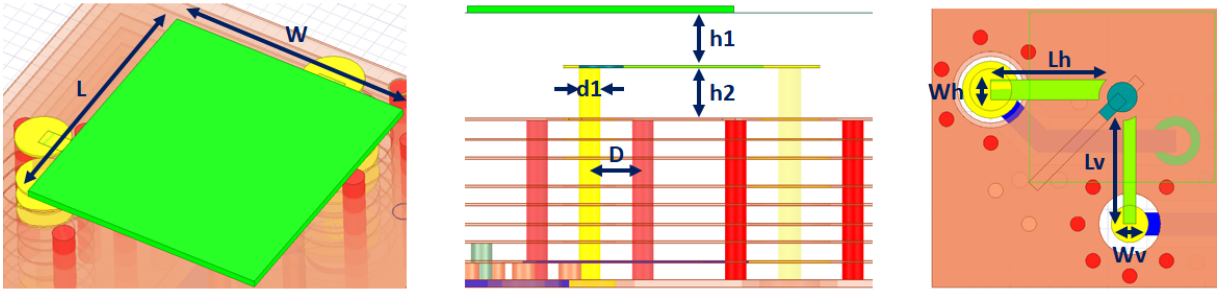


Figure 3.7: Dual-polarized proximity-coupled feed patch antenna design parameter

Table 3.2: Summary of design parameter of dual-polarized unit cell patch antenna.

Parameter	Description	Value	Unit
W	Patch Width	1.9	mm
L	Patch length	1.75	mm
h1	Height between feed and patch (after lamination)	14.82	mil
h2	Height between feed and ground (after lamination)	14.19	mil
d1	Coaxial feed transition diameter	6.5	mil
D	Center-to-center distance between signal to shielding via	26	mil
Lh	Microstrip feed line length (H-pol)	1.2	mm
Wh	Microstrip feed line width (H-pol)	5	mil
Lv	Microstrip feed line length (V-pol)	1.2	mm
Wv	Microstrip feed line width (V-pol)	8	mil

### 3.3 Array Design

After finishing the optimization on unit cell design, it can be scaled up to antenna array with desired size. In this section, two design variations of 4x4 dual-polarized phased array are presented, as well as the simulation results.

### 3.3.1 Decoupling Structure

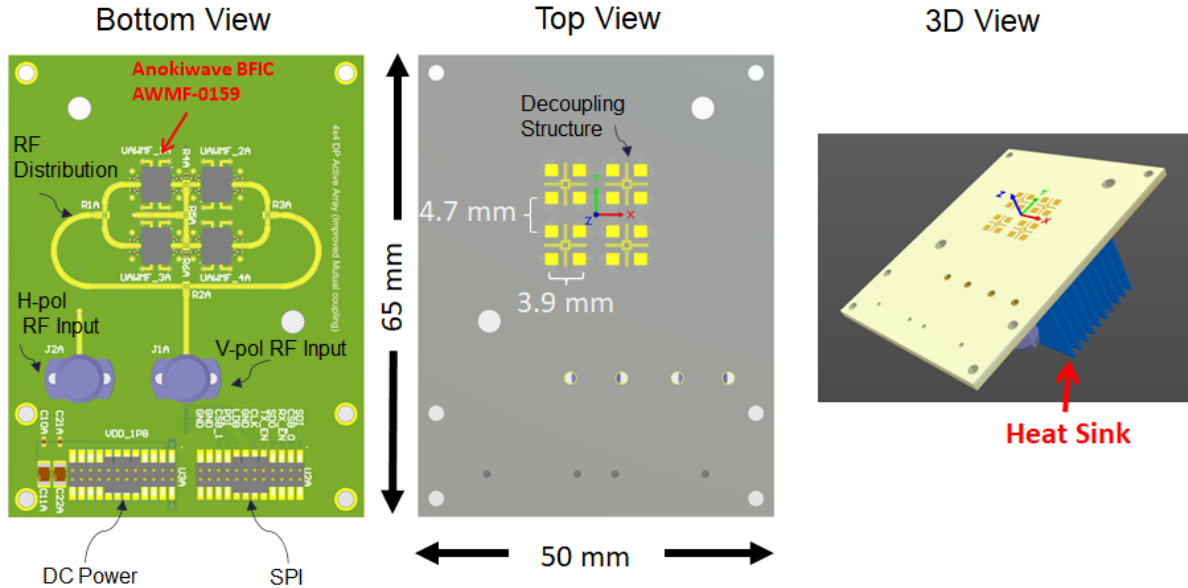


Figure 3.8: Overview of 4x4 dual-polarized phased array board with decoupling structure

Mutual coupling is an undesired interchange of energy between antenna elements in the phased array, which can significantly degrade overall radiation characteristics. When antennas are transmitting, part of the energy will be received by the other elements due to space waves, higher order wave, surface waves and leaky waves [32]. In literature, several methods to suppress the mutual coupling between antenna elements were introduced, such as defected ground structures (DGSs) [47], [48], complementary split-ring resonator (CSRR) [49], electromagnetic bandgap structures (EBGs) [50] and metamaterials [51]. A novel cross-shaped decoupling structure consists of four  $\pi$ -shaped coupled-line resonators that has bandstop effect is presented in this subsection, as well as simulated results of completed 4x4 dual-polarized phased array.

Fig. 3.8 displays the overview of 4x4 dual-polarized phased array board with decoupling structure. Four 37-40 GHz Anokiwave qual-channel BFICs are soldered on the bottom layer. There are two vertical 2.4 mm connectors for RF inputs, then the common RF signals are splitted into 4 channels for each polarization through Wilkinson distribution

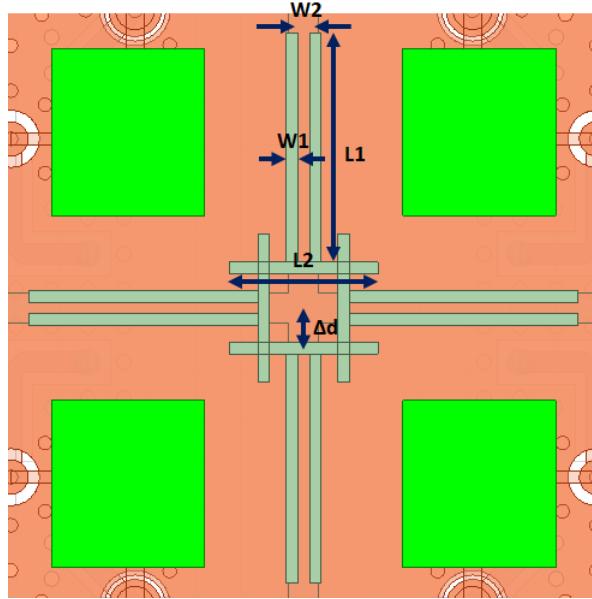
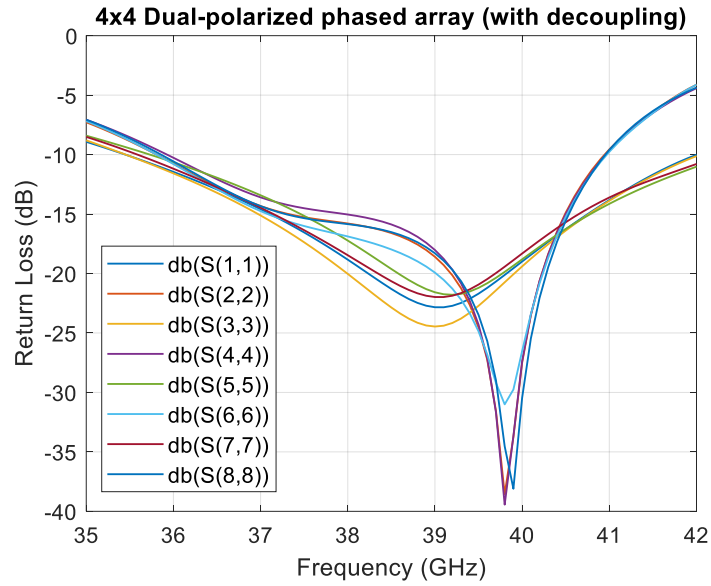


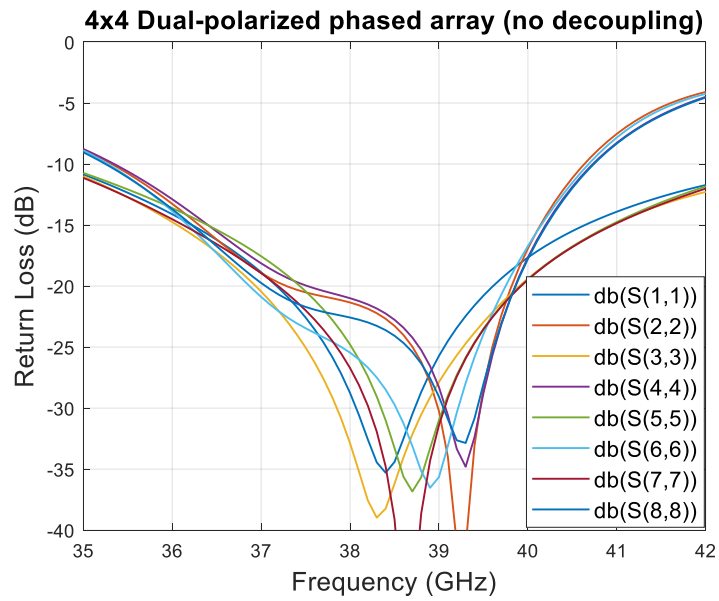
Figure 3.9: Geometry of decoupling structure

networks. SPI and power headers (24-pin, 50-mil pitch) are also surface-mounted at bottom layer. The overall board size is 50 mm x 65 mm and the distance between the elements within each 2x2 sub-array is 3.9 mm which is half of the wavelength at 38.5 GHz. However, the spacing between each 2x2 subarray has to increase to 4.7 mm ( $0.6\lambda$  @38.5 GHz) to accommodate bulky Wilkinson networks at the bottom layer. The cross-shaped decoupling structure is placed at the center of each 2x2 subarray. Lastly, a heat sink is assembled at the bottom of PCB to alleviate overheating of BFICs.

The decoupling structure is constructed at the same layer of radiation patch, the geometry consists of four  $\pi$ -shaped mirrored around center of 2x2 subarray, with each consisting of three coupled lines, as shown in Fig. 3.9. The optimized dimension of the decoupling structure are  $W1 = 5$  mil,  $W2 = 10$  mil,  $L1 = 100$  mil,  $L2 = 65$  mil,  $\Delta d = 20$  mil. To verify the effect of decoupling structure on the antenna resonant frequency, S-parameters of 4x4 dual-polarized phased arrays with and without decoupling structure deployed are simulated, as illustrated in Fig. 3.10. Only the results from the top-left subarray are displayed due to the symmetrical geometry. The input matching becomes slightly worse after

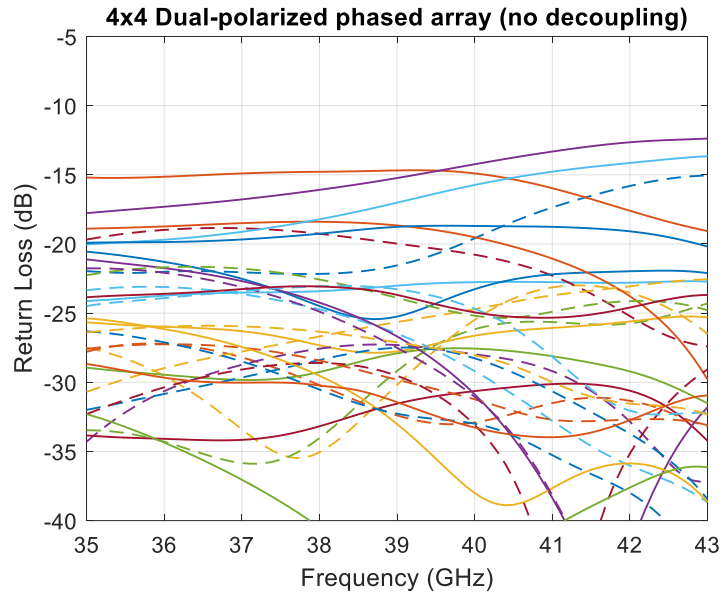


(a)

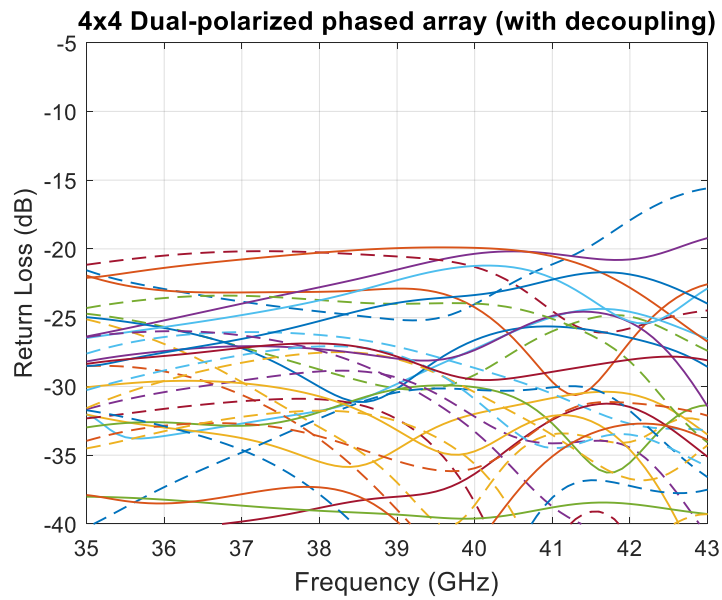


(b)

Figure 3.10: Simulated input matching of 4x4 dual-polarized phased array: (a) with decoupling structure (b) without decoupling structure



(a)



(b)

Figure 3.11: Simulated mutual coupling of 4x4 dual-polarized phased array: (a) with decoupling structure (b) without decoupling structure

adding the decoupling structures, while the -10 dB bandwidth remains the same which is from 35.5-42 GHz for V-pol and 36-41 GHz for H-pol. The advantage of mutual coupling suppression outweighs this minor drawback which can be seen from Fig. 3.11, decoupling structure provides additional 5 dB improvement in the element isolation and manages to suppresses all the mutual coupling level below -20 dB. The same effect can also be reflected from surface wave distribution, as illustrated in Fig. 3.12. It is evident that the surface current generated from excited antenna (top-left) is blocked by decoupling structure from reaching the adjacent elements.

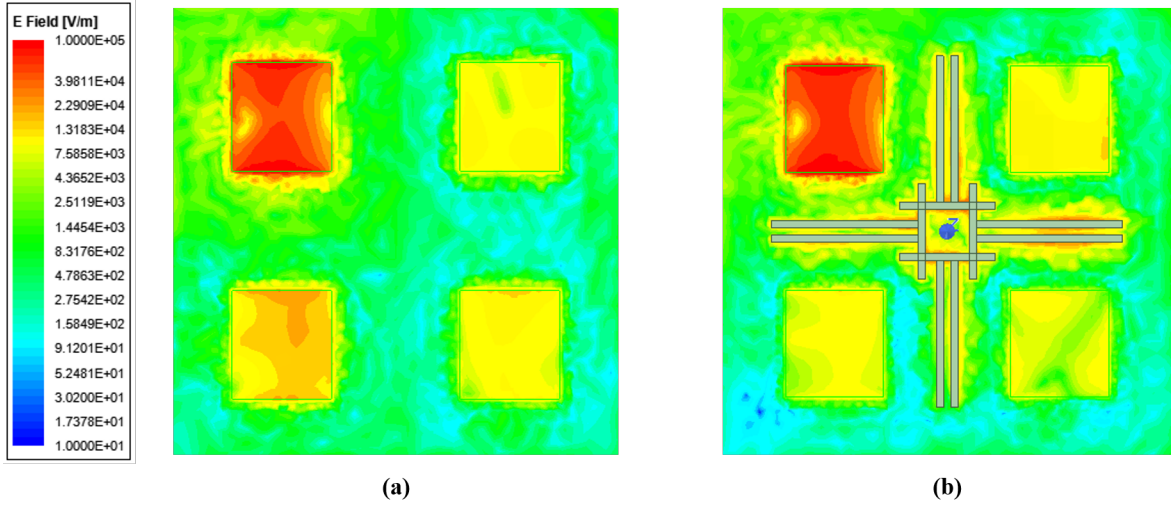


Figure 3.12: Simulated surface current distribution: (a) with decoupling structure (b) without decoupling structure

So far, the simulation results is obtained under the condition that only a single element of an array is excited with all other elements of the array passively terminated with nominal value of  $50 \Omega$  impedance. However, the total contribution to the FF pattern of a particular element in the array depends upon, not only its own excitation, but also the mutual coupling from the excitation of all other elements. Therefore, to fully validate the usefulness of design phased array, one should also observe active S-parameters which the equation is given as follows:

$$AS_{11}[dB] = 20 \log_{10} \left| \frac{S_{11} * a_1 + S_{12} * a_2 + \dots + S_{1n} * a_n}{a_1} \right| \quad (3.1)$$

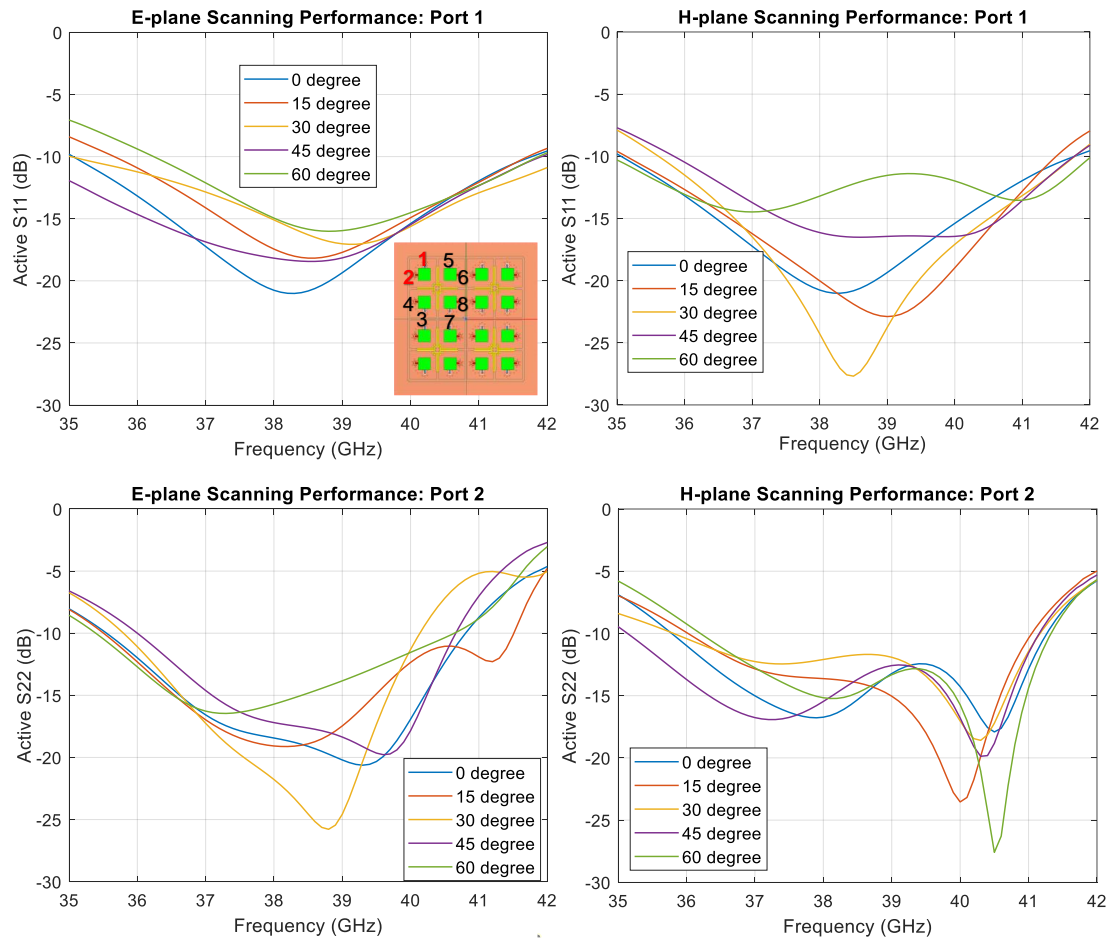


Figure 3.13: Simulated Active S-parameters of corner elements.

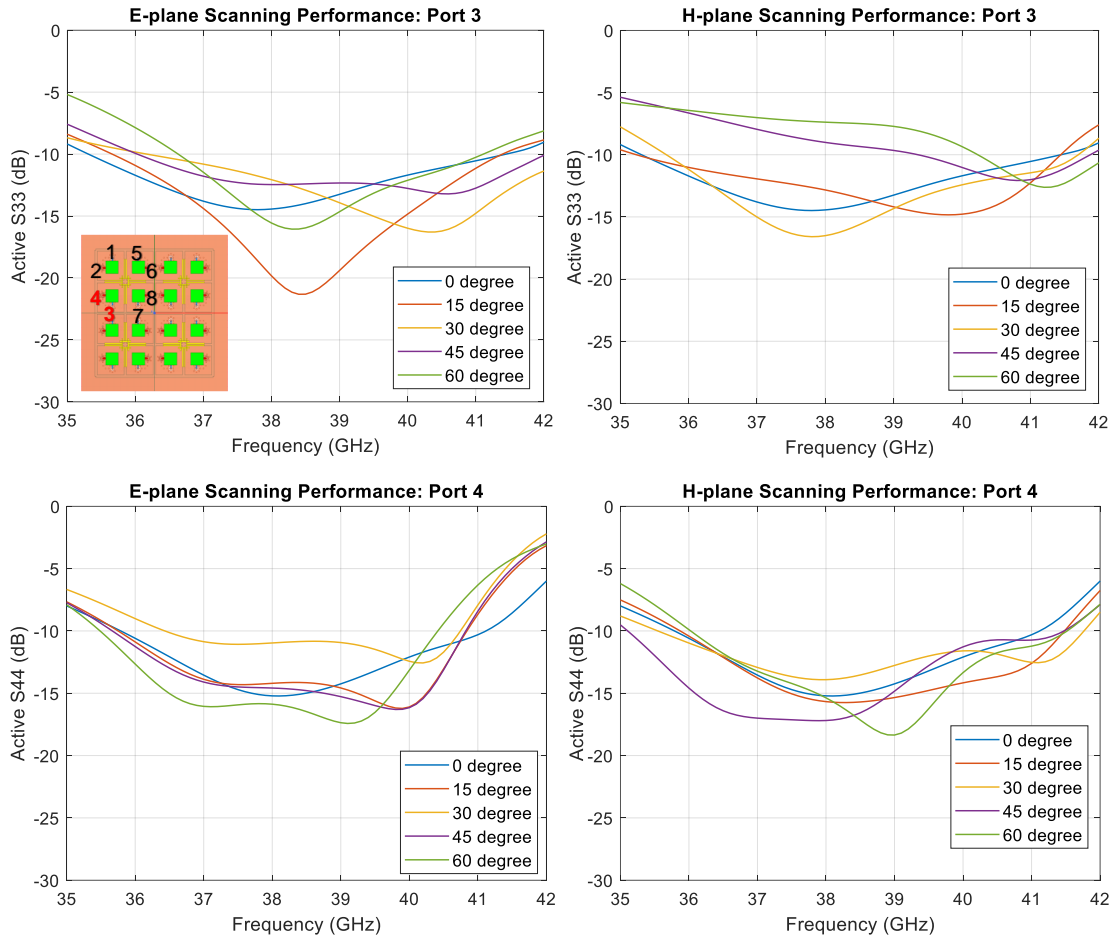


Figure 3.14: Simulated Active S-parameters of edge elements.

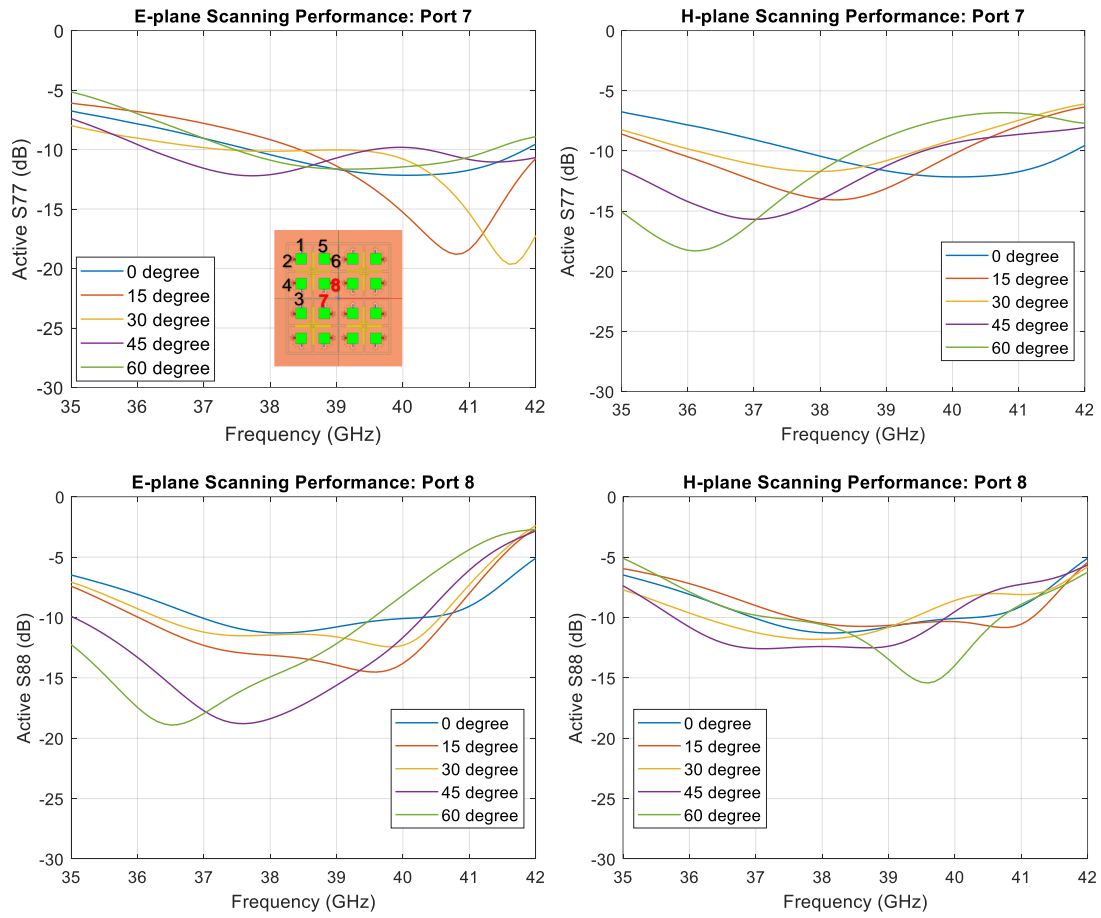


Figure 3.15: Simulated Active S-parameters of middle elements.

where  $S_{1n}$  is the complex mutual coupling value between  $1st$  element and  $nth$  element, and  $a_n$  is the complex excitation in volts incident in  $nth$  element. Fig. 3.13 - Fig. 3.15 present the comprehensive EM simulated active S-parameters of the elements at the corner, edge and middle, as the array scans to  $60^\circ$  for both H- and E- planes. It can be observed that, the elements are still well-matched with active S11 less than -10 dB with the array scanning on both planes. Among three different cases, the elements at the middle have the worst performance, because they have shorter distances to the remaining elements which means the mutual coupling is relatively stronger.

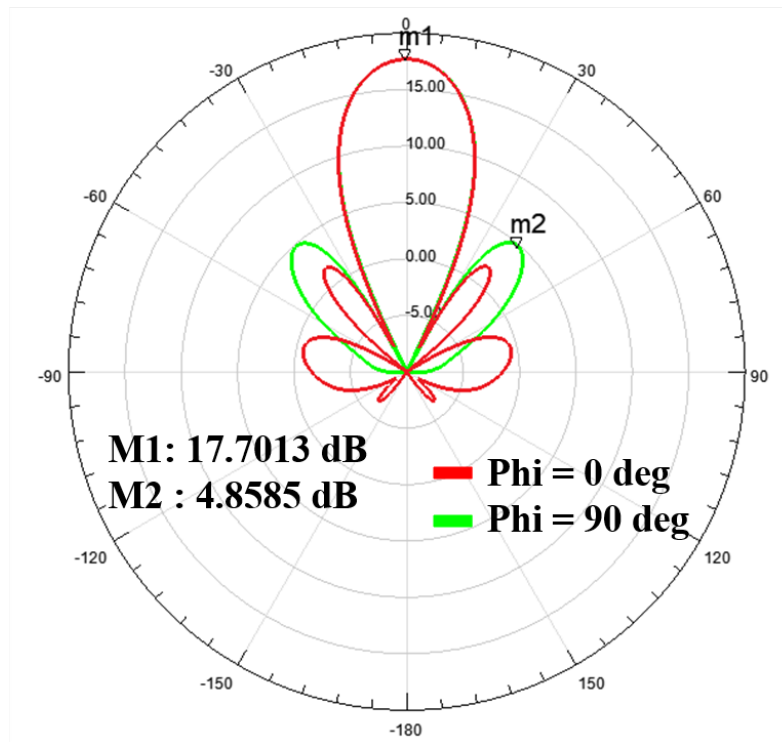


Figure 3.16: Simulated radiation pattern at boresight for V-pol @ 38.5 GHz

Another fundamental parameter to assess the performance of a phased array antenna is radiation pattern, it describes a graphical representation of the radiation properties of the antenna as a function in space coordinates. Some useful properties that one can obtain from radiation pattern are directivity, half-power bandwidth (HPBW), main lobe level and

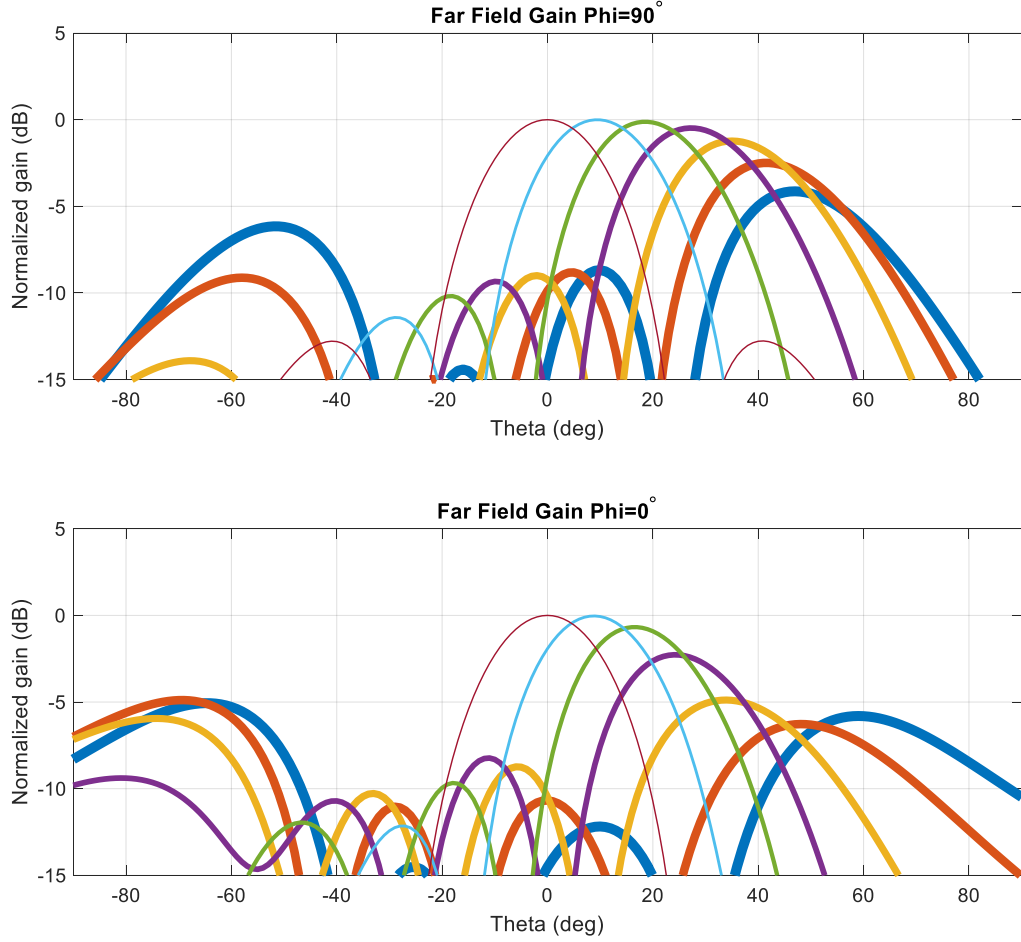


Figure 3.17: Simulated normalized radiation pattern for H-pol when scanned to  $\pm 60^\circ$  @ 38.5 GHz

side lobe levels. In addition, the maximum antenna gain of designed phased array can be calculated as follows:

$$G_{\text{array}} = G_{\text{element}} + 10 \log_{10}(N) = 16.43 \text{ dB}|_{38.5 \text{ GHz}} \quad (3.2)$$

where  $N$  is the total number of elements in the array which equals to 16 in this design.  $G_{\text{element}}$  is the antenna gain of single element which can also be estimated as follows:

$$G_{\text{element}} = 10 \log_{10} \left( \frac{4\pi D_x D_y}{\lambda^2} \right) = 4.39 \text{ dB}|_{38.5 \text{ GHz}} \quad (3.3)$$

where  $D_x$  and  $D_y$  are the physical dimensions of the patch. Fig. 3.16 displays the simulated radiation pattern at boresight in polar coordinate system with V-pol excited. The main lobe is pointing in the  $\theta = 0$  direction with maximum 17.7 dB array gain which is higher than estimation, and  $23^\circ$  HPBW. Because the fringing effect makes the effective dimensions slightly larger than the actual physical size. The side lobes, represent radiation in undesired directions, appears at  $\pm 42^\circ$  with around 13 dB lower than the main lobe. It is mainly due to the sub-optimal spacing between each 2x2 subarray. To better observe the beam angle scanning capability, radiation patterns are often normalized with respect to their maximum value, as shown in Fig. 3.17. When H-pol is excited, no grating lobe can be observed and side lobe level remains below -8 dB as array scans to  $\pm 50^\circ$  and  $\pm 30^\circ$  in E- and H-plane at 38.5 GHz, respectively. Besides the  $0.6\lambda$  distance between 2x2 subarray, the tilted radiation pattern of single element due to the asymmetrical geometry degrades the scan range on the H-plane for H-pol.

### 3.3.2 Near-Field Probe

To perform DPD techniques on phased array for compensating the nonlinearity exhibited by PAs at sub-6 GHz, directional couplers are usually implemented between each PA and antenna element to acquire the PAs output. However, it is challenging to apply the same approach for mm-wave phased array given the compact BFICs size and high system integration level. Alternatively, FF-based probe (typically horn antenna) can be used to receive the FF signal to estimate the individual PAs output which is also a conventional method for array calibration. Unfortunately, FF probe is not always available in real-world scenario. As an attempt to address the problem associated with coupler- and FF-based DPD/array calibration, this subsection proposes a NF-based probe embedded in the transmitter phased array.

The overview of 4x4 dual-polarized phased array board with NFPs is displayed in Fig. 3.18, four NFPs are uniformly distributed among array with each placed in the centre

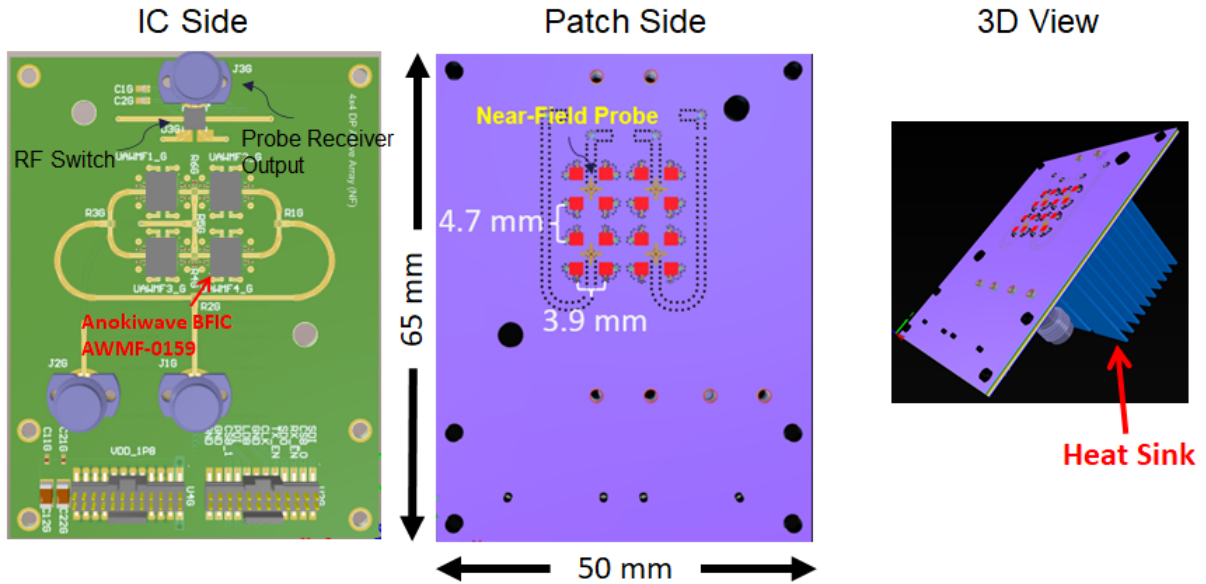


Figure 3.18: Overview of 4x4 dual-polarized phased array board with NFPs

of 2x2 subarray. This kind of arrangement utilizes mutual coupling and ensures similar coupling magnitude and phase between the NFP and four nearest surrounding antenna elements. The proposed approach maintains the uniformity and does not hinder the scalability of phased array from expanding to any desired size. Each NFP can be treated as a variant of coaxial-fed patch antenna, consists of a cross-shaped coupled branch and a coaxial-like structure with four fencing ground vias. The NFP is located at the second layer, connected to a single-pole four-throw (SP4T) switch through stripline at layer 6 and two sets of via transition (2:7 & 2:13), then the near-field output signal can be captured through a RF connector as receiver.

To fully take advantage of 5G mm-wave spectrum, signal with multiple hundreds of MHz bandwidth and complex modulation modes are used. Moreover, the sampling speed of DPD engine training typically calls for several times of modulated signal bandwidth to improve signal to noise ratio (SNR). This is to confirm the quality of sampled signal by verify if the received signal from NFP is the exact copy of the signal that was fed to phased array. Now it is evident that when integrating the NFP into array, there are two important

criteria. The first is an obvious one that the additional probes must not disturb the overall array performance. The second one is, the coupling magnitude and group delay between NFP and radiation elements needs to be flat over one GHz in the required frequency range. The simulated result is displayed in Fig. 3.19, where not only proves that the designed NFP couples to both polarization, but also has flat coupling magnitude and group delay over the operating frequency band.

To further prove the validity of NFP design, by the co-simulation of HFSS and MATLAB, each element was excited with an 5G 800-MHz wide 256 QAM (quadrature amplitude modulation) OFDM signal with 11 dB PAPR centered at 38.5 GHz which the detail is listed in the Table. 3.3. As summarized in Fig. 3.20, the normalized root mean square error (NMSE) of received modulated signal by NFP from four surrounding radiation elements are around 1 and error vector magnitudes (EVM) are at the order of 0.01 %. These results verifies that the design of the antenna and the near-field probes function as intended.

Table 3.3: Detail of modulated signal used in simulation.

<b>Device under test (DUT)</b>	16-element dual-polarized phased array with NFPs
<b>Frequency</b>	38.5 GHz
<b>Signal Modulation BW</b>	800 MHz
<b>Signal Modulation</b>	256 QAM, OFDM (after lamination)
<b>Sub Carrier Spacing</b>	120 KHz (after lamination)
<b>Cyclic Prefix Length</b>	1/16 the FFT Length
<b>Sampling Rate</b>	4 GHz
<b>Oversampling</b>	5x
<b>PAPR</b>	11 dB
<b>Signal Length</b>	144000

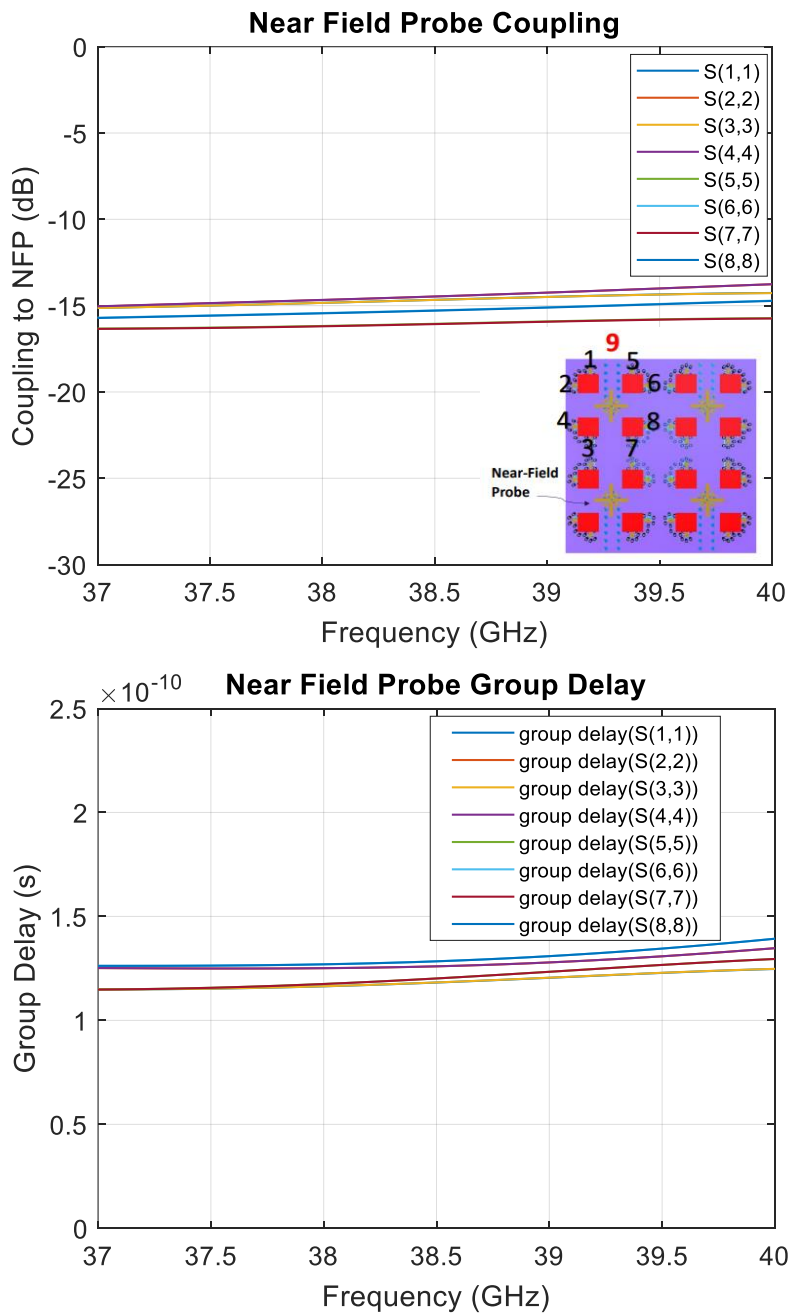


Figure 3.19: Simulated magnitude and group delay of coupling between NFP and surrounding antenna elements

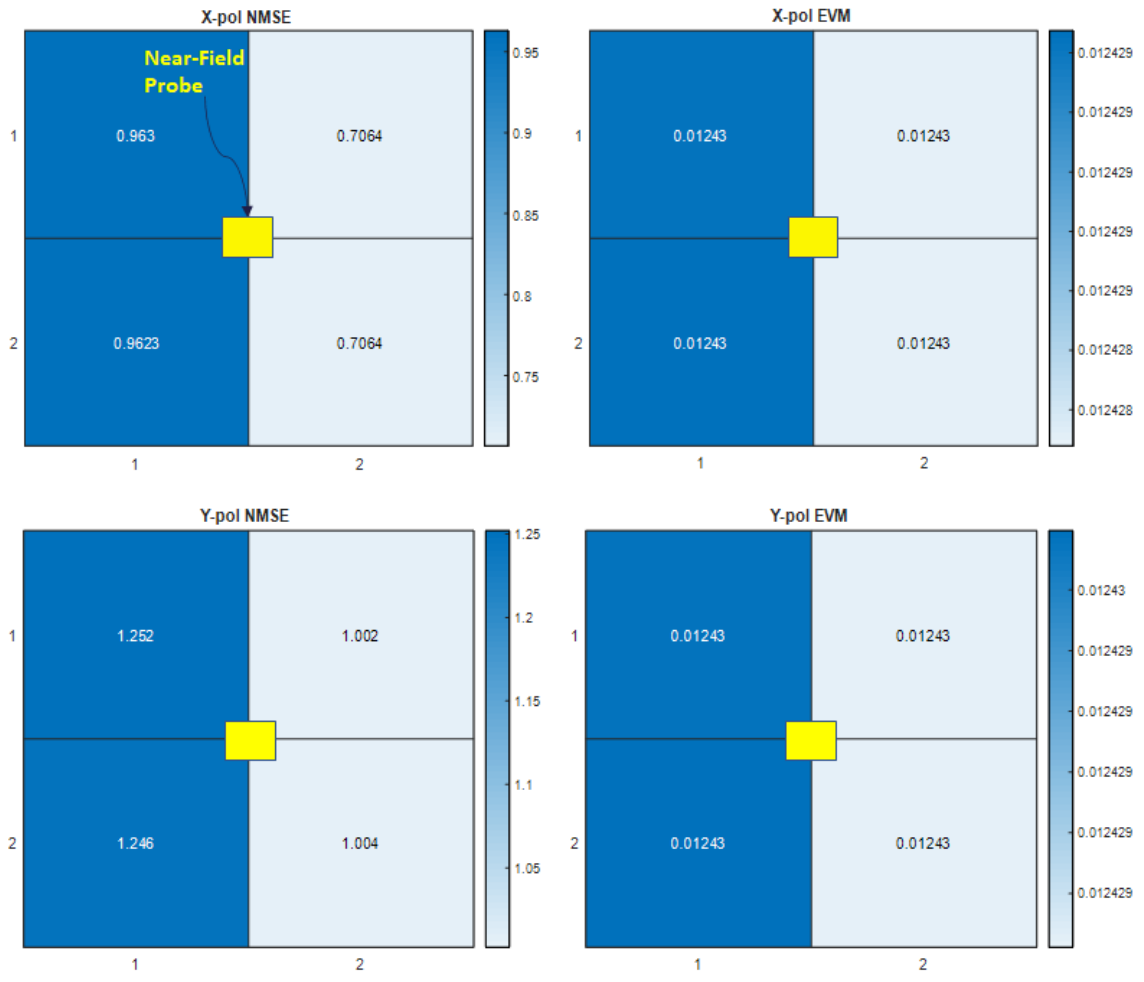


Figure 3.20: Simulated NMSE and EVM of received modulated signal from NFPs

# Chapter 4

## Experimental Validation

Two 37-40 GHz 16-element dual-polarized beamforming arrays, one with decoupling structure and another with near-field probe were fabricated and assembled for experimental validation. Due to time constraints, only the continuous-wave measurements (CW) of the phased array with decoupling structure were finished and the rest are still in progress at the time of writing this thesis.

### 4.1 Measurement Setup

As shown in Fig. 4.1, the 16-element dual-polarized phased array with decoupling structure was measured in an anechoic chamber using a Keysight N5247B VNA and two horn antennas placed at far-field region (120 cm) as receivers. The array board was assembled on a adaptor board which was fixed on a rotateble motor. The array was controlled by using USB-8452 interface device from National Instruments and MATLAB for the SPI commands.

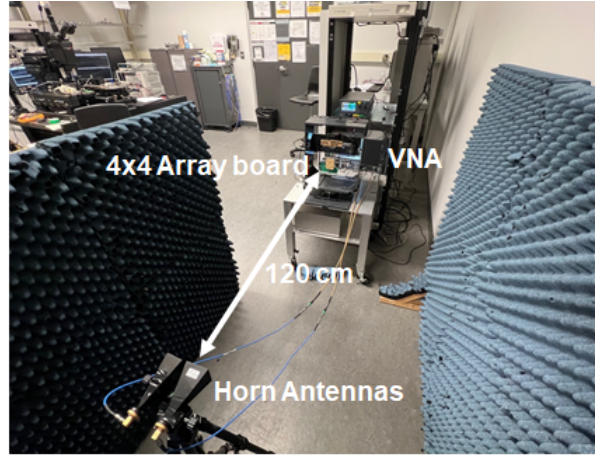
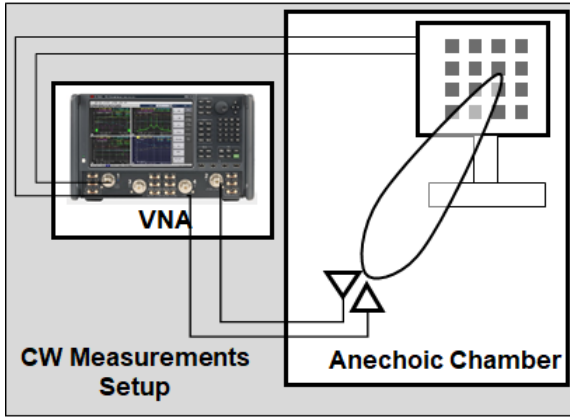


Figure 4.1: CW Measurement setup

## 4.2 Beamforming Array Assessment

### 4.2.1 Array Calibration

Residual amplitude and phase errors exist among all the transmitter channels due to channel-to-channel and chip-to-chip variations of BFICs. Furthermore, the transmission line length difference and asymmetrical Wilkinson divider networks caused by manufacture tolerance aggravate amplitude and phase errors. Therefore, array calibration needs to be performed by adjusting gain and phase state of each Tx channel in BFICs.

For the amplitude calibration, each channel was excited one at a time with all 64 phase states (6-bit phase control), and the respective power level received by horn antennas was measured by VNA. Since the BFICs from Anokiwave use RF variable attenuators as gain control, the reference power level was chosen at minimum + 2 dB for the purpose of not sacrificing too much power. In another words, for all the channels that have power higher than reference level need to decrease to reference level. Then each element was measured again after the magnitude offset was applied. Fig. 4.2 shows the measured magnitude difference between 16 elements with 64 phase state before and after magnitude calibration

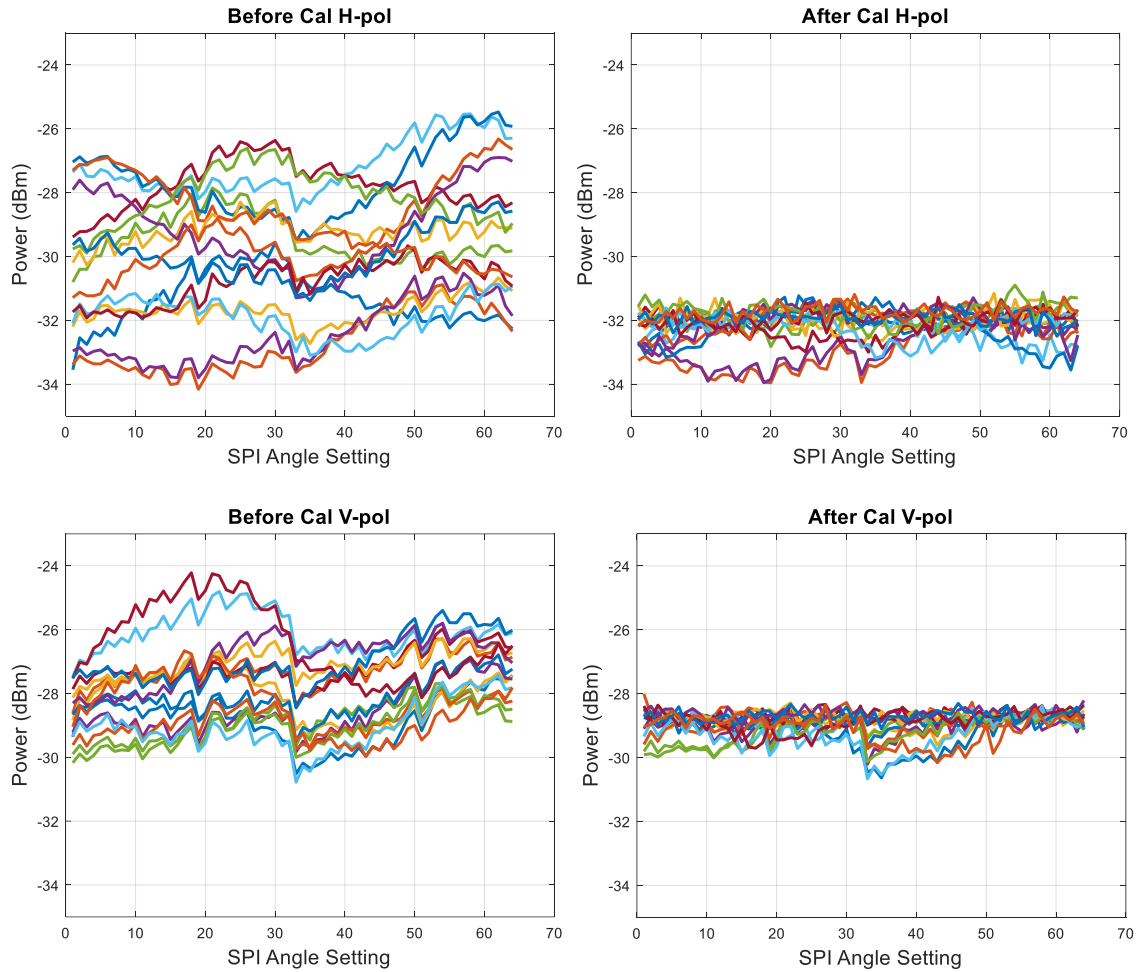


Figure 4.2: Gain variation before and after calibration

for both V- and H-pol at 38.5 GHz. The magnitude variations decrease from 7.6 dB and 5.7 dB to 2.4 dB and 2.1 dB after magnitude calibration for the H- and V-pol, respectively.

The procedure for phase calibration is similar, Fig. 4.3 summarized the measured phase variation after calibration at 38.5 GHz as heat maps. For both polarizations, the top-left element was selected as reference for phase calibration. It can be seen that the highest offset is  $4.042^\circ$  and  $4.144^\circ$  for V- and H-pol which are lower than least-significant-bit resolution ( $5.625^\circ$ ).

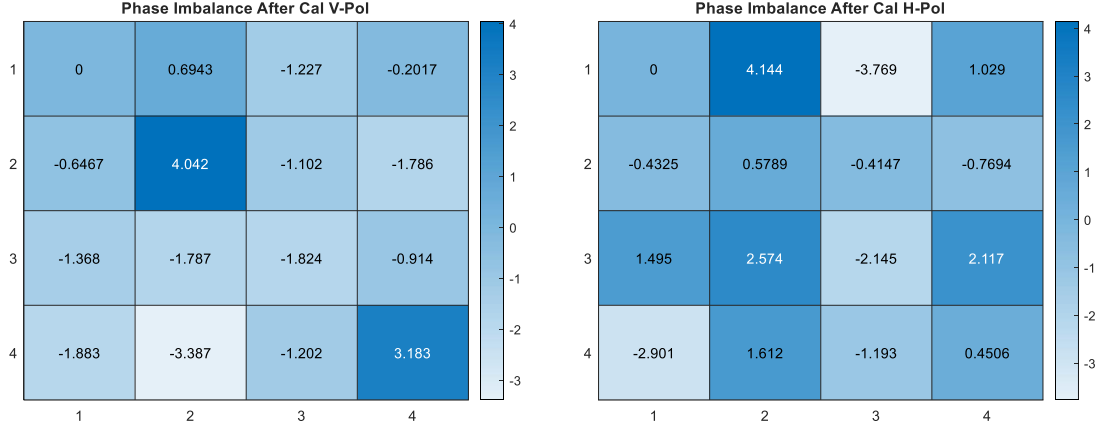


Figure 4.3: Phase variation after calibration

## 4.2.2 Frequency Response

Fig. 4.4 shows the measured frequency response at boresight with uniform illumination with four different cases, before calibration, after full calibration (phase + magnitude), after phase calibration only and after magnitude calibration only, each is normalized to the peak value of them. The overall shapes of frequency responses are similar for all four cases. The 3-dB bandwidth is 36.7 - 41.1 GHz and 37.2 - 41.2 for H- and V-pol. For the cases of full calibration and magnitude calibration only, it can be observed about 4 dB power reduction compare to phase calibration only and before calibration.

## 4.2.3 Radiation Pattern

Fig. 4.5 shows the measured radiation pattern at boresight for V- and H-pol in horizontal plane at 38.5 GHz with three different cases, before calibration, after full calibration and after phase calibration only, each is normalized to its peak value. This is done by fixing the physical location of horn antenna and motor at  $\theta = 0^\circ$ , then electrically scan the beam from  $-60^\circ$  to  $60^\circ$  in horizontal plane. Before calibration, the radiation patterns are not symmetrical around  $\theta = 0^\circ$ . After phase only and full calibration, the radiation patterns

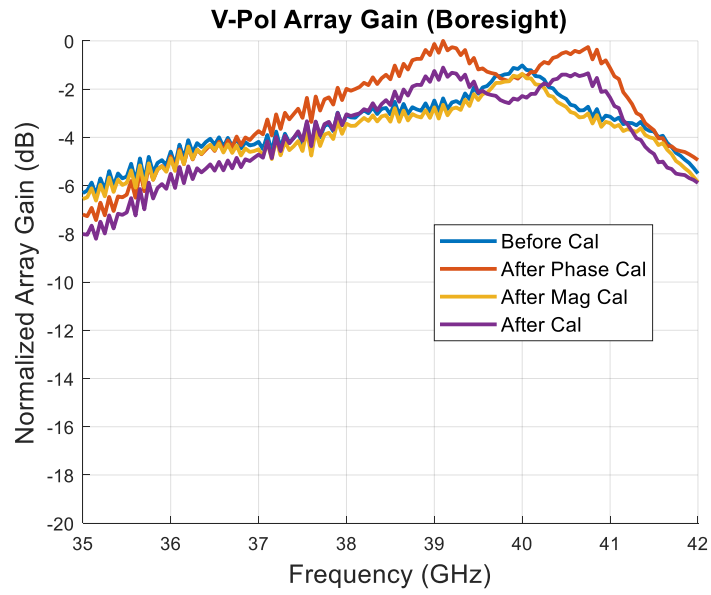
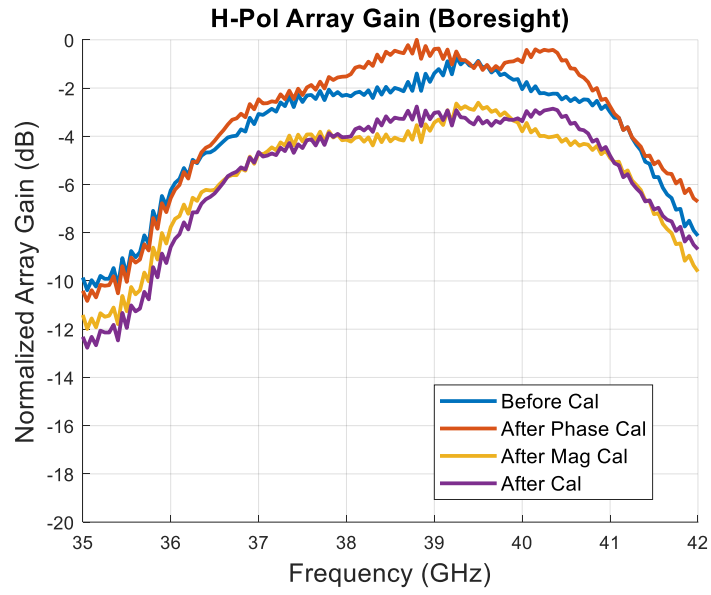


Figure 4.4: VNA S-parameters measurements

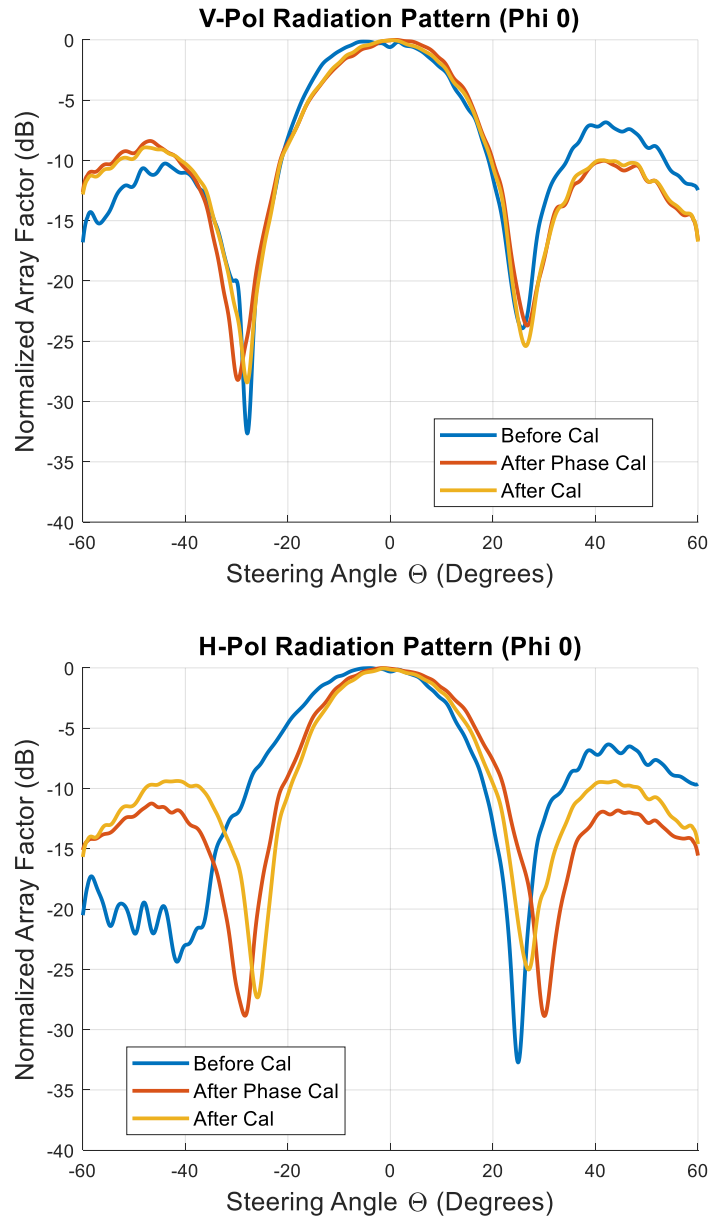


Figure 4.5: Measured pattern at boresight in horizontal plane at 38.5 GHz

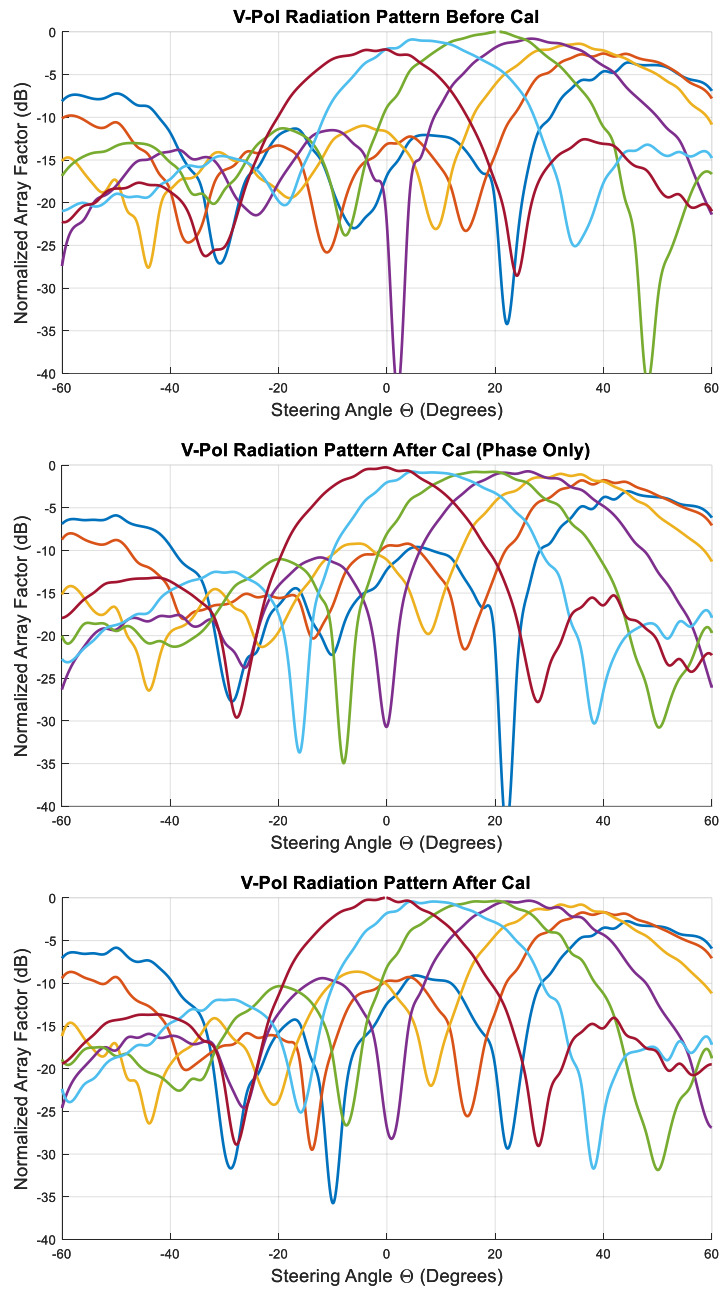


Figure 4.6: Measured pattern with  $-60^\circ$  to  $60^\circ$  for V-pol in horizontal plane at 38.5 GHz

become more symmetrical and side lobes occurs at about  $\pm 42^\circ$  with level of -14 to -10 dB. In addition, the main lobe has  $23^\circ$  HPBW which matches to the simulation results.

The radiation pattern with beam angle scanned in horizontal plane at 38.5 GHz was measured to further assess phased array performance, as displayed in Fig. 4.6 and Fig. 4.7. This is done by setting the beam angle fixed but rotating the motor from  $-60^\circ$  to  $60^\circ$  in horizontal plane. Before calibration, the maximum amplitude does not occur at uniform illumination. After calibration, the array is capable of scanning to  $\pm 50^\circ$  without significant side lobes. The same scanning performance can be also obtained by phase calibration but without any power compromise. Therefore, it is suggested that phase calibration is sufficient and should be implemented for array calibration. The Horizontal plane pattern for H-pol is good up to  $20^\circ$  scan, mainly due to the non-optimal subarray spacing and asymmetrical unit cell radiation pattern. The scanned radiation pattern for H-pol is similar to that of V-pol which is not shown here.

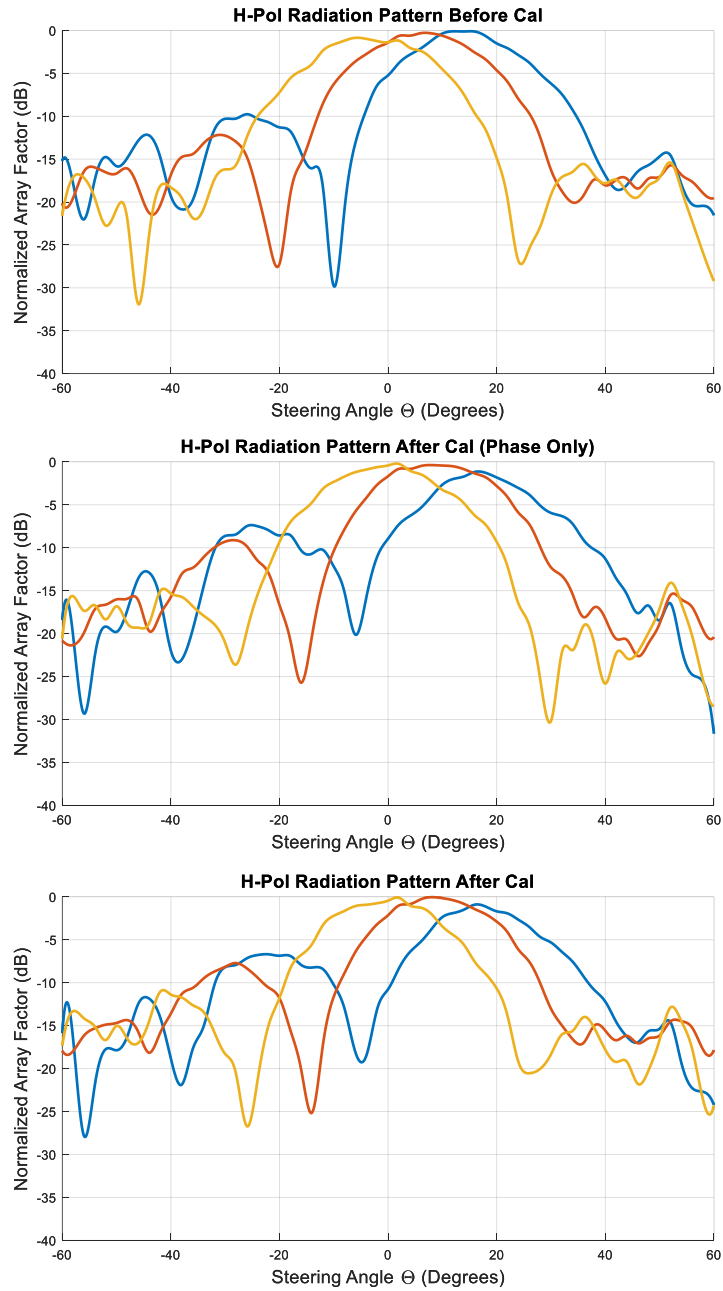


Figure 4.7: Measured pattern with  $-20^\circ$  to  $20^\circ$  for H-pol in horizontal plane at 38.5 GHz

# Chapter 5

## Conclusion and Future Works

### 5.1 Conclusion

As introduced in Chapter 1, sub-6 GHz band is already occupied by many existing applications, mm-wave becomes more attractive for researchers as it provides more spacious and wider bandwidth for higher data rates. Although beamforming array has been proved to be a promising solution to compensate high FSPL at mmWave bands, a more practical feedback path realization is desired for array calibration and DPD training.

Chapter 2 first briefly explained some background theory of phased array and different beamforming architectures, RF (Analog) beamforming is relatively easy to implement and the still most widely used so far. Then three different approaches to construct the beamforming phased array was reviewed; antenna-on-pcb has low manufacture cost, low complexity and ease of expanding to larger size which made it appropriate to the design in this thesis, even though antenna-in-package and antenna-on-chip can provide high system integration level. Next, several attempts to utilize mutual coupling and built-in feedback path for DPD and array calibration in literature was surveyed.

In Chapter 3, a low-cost antenna-on-pcb based 37-40 GHz dual-polarized phased array with embedded NFPs which eliminates the need of impractical FF-based probe for calibration and DPD was proposed. Antenna element as well as feeding mechanism and PCB

stackup was discussed. Based on the optimization of unit cell, two phased arrays were designed and simulated, one with decoupling structure, and the other with NFPs. The array achieved at least -10 dB bandwidth for both polarizations over 36-41 GHz . The decoupling structure helped to improve 5 dB mutual coupling level. Based on simulated radiation pattern, the array could achieve maximum 17.7 dB antenna gain with a scan angle of  $\pm 50^\circ$ ,  $\pm 30^\circ$  in azimuth and  $\pm 30^\circ$ ,  $\pm 50^\circ$  in elevation for vertical polarization and horizontal polarization, respectively. The uniformly distributed NFP was designed at the centre of each 2x2 subarray so the array size is not limited. Each NFP has flat coupling magnitude and group delay to the surrounding four elements to ensure the received signal quality. An 800 MHz OFDM modulated signal was used to simulate EVM and NMSE of received signal, resulted in 1 and 0.012 %, respectively. The simulated results proved the capability of proposed NFP to serve as embedded feedback path for array calibration and DPD.

Chapter 4 reported the measured results of fabricated phased array boards. Due to time constraints, only CW tests of the phased array with decoupling structure were finished and the rest are still in progress at the time of finishing this thesis. The measurement result showed 36.7 - 41.1 GHz and 37.2 - 41.2 GHz of 3-dB bandwidth for H- and V-pol. Because assembled BFICs use variable attenuators as gain control, there was about 4 dB power reduction after magnitude calibration and full calibration (Magnitude + Phase). At 38.5 GHz, for H-plane pattern, V-pol achieved  $\pm 50^\circ$  beam angle scanning without significant side lobes, while H-pol was limited by non-optimum subarray spacing and asymmetrical unit cell radiation. All the measurement results obtained so far matched well with simulation results.

## 5.2 Future Works

Other than finishing the rest of measurements to fully prove the validity of proposed design, there are some potential future works require further investigation.

For now, the spacing between each 2x2 subarray is  $0.6\lambda$  at 38.5 GHz because of the bulky Wilkinson network at bottom layer which deteriorates the scanning range. As a major

improvement in next stage, Wilkinson networks with buried resistor will be implemented so the BFIC can be placed closer so that the optimal  $0.5\lambda$  spacing will be maintained for all the elements. In addition, NFP and decoupling structure were designed on two separate phased array boards in this thesis as an initial proof-of-concept. To fully take the advantage of them, one of the future works on this subject is to design NFP and decoupling structure on the same phased array, or even, to design a unified structure used for both NFP and mutual coupling suppression.

Since phased array is expected to be an integral part in future wireless communication where the same hardware can be repurposed for terrestrial and non-terrestrial communication or can be deployed to the countries with different allocated frequency bands, dual-band or wideband phased array with NFP still worth more research effort.

# References

- [1] “Wireless spectrum is for sale but what is it?” Available at <https://theconversation.com/wireless-spectrum-is-for-sale-but-what-is-it-11794>.
- [2] “mmWave 5G devices powered by Qualcomm Snapdragon can deliver 4x faster 5G,” Available at <https://www.qualcomm.com/news/onq/2020/06/mmwave-5g-devices-powered-qualcomm-snapdragon-can-deliver-4x-faster-5g>.
- [3] S. Shahramian, M. J. Holyoak, and Y. Baeyens, “A 16-Element W-Band Phased-Array Transceiver Chipset With Flip-Chip PCB Integrated Antennas for Multi-Gigabit Wireless Data Links,” *IEEE Transactions on Microwave Theory and Techniques*, vol. 66, no. 7, pp. 3389–3402, 2018.
- [4] T. Sowlati, S. Sarkar, B. G. Perumana, W. L. Chan, A. Papio Toda, B. Afshar, M. Boers, D. Shin, T. R. Mercer, W.-H. Chen, A. Grau Besoli, S. Yoon, S. Kyriazidou, P. Yang, V. Aggarwal, N. Vakilian, D. Rozenblit, M. Kahrizi, J. Zhang, A. Wang, P. Sen, D. Murphy, A. Sajjadi, A. Mehrabani, E. Kornaros, K. Low, K. Kimura, V. Roussel, H. Xie, and V. Kodavati, “A 60-GHz 144-Element Phased-Array Transceiver for Backhaul Application,” *IEEE Journal of Solid-State Circuits*, vol. 53, no. 12, pp. 3640–3659, 2018.
- [5] M. Boers, B. Afshar, I. Vassiliou, S. Sarkar, S. T. Nicolson, E. Adabi, B. G. Perumana, T. Chalvatzis, S. Kavvadias, P. Sen, W. L. Chan, A. H.-T. Yu, A. Parsa, M. Nariman, S. Yoon, A. G. Besoli, C. A. Kyriazidou, G. Zochios, J. A. Castaneda, T. Sowlati, M. Rofougaran, and A. Rofougaran, “A 16TX/16RX 60 GHz 802.11ad

- Chipset With Single Coaxial Interface and Polarization Diversity,” *IEEE Journal of Solid-State Circuits*, vol. 49, no. 12, pp. 3031–3045, 2014.
- [6] B.-H. Ku, P. Schmalenberg, O. Inac, O. D. Gurbuz, J. S. Lee, K. Shiozaki, and G. M. Rebeiz, “A 77–81-GHz 16-Element Phased-Array Receiver with  $\pm 50^\circ$  Beam Scanning for Advanced Automotive Radars,” *IEEE Transactions on Microwave Theory and Techniques*, vol. 62, no. 11, pp. 2823–2832, 2014.
- [7] E. Cohen, M. Ruberto, M. Cohen, O. Degani, S. Ravid, and D. Ritter, “A Cmos Bidirectional 32-Element Phased-Array Transceiver at 60 GHz with LTCC Antenna,” *IEEE Transactions on Microwave Theory and Techniques*, vol. 61, no. 3, pp. 1359–1375, 2013.
- [8] S. Shahramian, M. J. Holyoak, A. Singh, and Y. Baeyens, “A Fully Integrated 384-Element, 16-Tile, W-Band Phased Array With Self-Alignment and Self-Test,” *IEEE Journal of Solid-State Circuits*, vol. 54, no. 9, pp. 2419–2434, 2019.
- [9] B. Sadhu, Y. Tousi, J. Hallin, S. Sahl, S. K. Reynolds, Renström, K. Sjögren, O. Haapalahti, N. Mazor, B. Bokinge, G. Weibull, H. Bengtsson, A. Carlinger, E. Westesson, J.-E. Thillberg, L. Rexberg, M. Yeck, X. Gu, M. Ferriss, D. Liu, D. Friedman, and A. Valdes-Garcia, “A 28-GHz 32-Element TRX Phased-Array IC with Concurrent Dual-Polarized Operation and Orthogonal Phase and Gain Control for 5G Communications,” *IEEE Journal of Solid-State Circuits*, vol. 52, no. 12, pp. 3373–3391, 2017.
- [10] A. Townley, P. Swirhun, D. Titz, A. Bisognin, F. Gianesello, R. Pilard, C. Luxey, and A. M. Niknejad, “A 94-GHz 4TX–4RX Phased-Array FMCW Radar Transceiver With Antenna-in-Package,” *IEEE Journal of Solid-State Circuits*, vol. 52, no. 5, pp. 1245–1259, 2017.
- [11] H.-T. Kim, B.-S. Park, S.-S. Song, T.-S. Moon, S.-H. Kim, J.-M. Kim, J.-Y. Chang, and Y.-C. Ho, “A 28-GHz CMOS Direct Conversion Transceiver with Packaged  $2 \times 4$  Antenna Array for 5G Cellular System,” *IEEE Journal of Solid-State Circuits*, vol. 53, no. 5, pp. 1245–1259, 2018.

- [12] U. Kodak, B. Rupakula, S. Zehir, and G. M. Rebeiz, “60-GHz 64- and 256-Element Dual-Polarized Dual-Beam Wafer-Scale Phased-Array Transceivers With Reticule-to-Reticule Stitching,” *IEEE Transactions on Microwave Theory and Techniques*, vol. 68, no. 7, pp. 2745–2767, 2020.
- [13] G. Gültepe, T. Kanar, S. Zehir, and G. M. Rebeiz, “A 1024-Element Ku-Band SAT-COM Phased-Array Transmitter With 45-dBW Single-Polarization EIRP,” *IEEE Transactions on Microwave Theory and Techniques*, vol. 69, no. 9, pp. 4157–4168, 2021.
- [14] B. Rupakula, S. Zehir, and G. M. Rebeiz, “Low Complexity 54–63-GHz Transmit/Receive 64- and 128-element 2-D-Scanning Phased-Arrays on Multilayer Organic Substrates With 64-QAM 30-Gbps Data Rates,” *IEEE Transactions on Microwave Theory and Techniques*, vol. 67, no. 12, pp. 5268–5281, 2019.
- [15] Y. Yin, B. Ustundag, K. Kibaroglu, M. Sayginer, and G. M. Rebeiz, “Wideband 23.5–29.5-GHz Phased Arrays for Multistandard 5G Applications and Carrier Aggregation,” *IEEE Transactions on Microwave Theory and Techniques*, vol. 69, no. 1, pp. 235–247, 2021.
- [16] Y. Wang, T. Phelps, B. Rupakula, S. Zehir, and G. M. Rebeiz, “64 GHz 5G-Based Phased-Arrays for UAV Detection and Automotive Traffic-Monitoring Radars,” in *2019 IEEE International Symposium on Phased Array System Technology (PAST)*, 2019, pp. 1–4.
- [17] Y. Wang, R. Wu, J. Pang, D. You, A. A. Fadila, R. Saengchan, X. Fu, D. Matsumoto, T. Nakamura, R. Kubozoe, M. Kawabuchi, B. Liu, H. Zhang, J. Qiu, H. Liu, N. Oshima, K. Motoi, S. Hori, K. Kunihiro, T. Kaneko, A. Shirane, and K. Okada, “A 39-GHz 64-Element Phased-Array Transceiver With Built-In Phase and Amplitude Calibrations for Large-Array 5G NR in 65-nm CMOS,” *IEEE Journal of Solid-State Circuits*, vol. 55, no. 5, pp. 1249–1269, 2020.
- [18] M. Repeta, W. Zhai, T. Ross, K. Ansari, S. Tiller, H. K. Pothula, D. Wessel, X. Li, H. Cai, D. Liang, G. Wang, and W. Tong, “A Scalable 256-Element E-Band Phased-

- Array Transceiver for Broadband Communications,” in *2020 IEEE/MTT-S International Microwave Symposium (IMS)*, 2020, pp. 833–836.
- [19] X. Gu, D. Liu, C. Baks, O. Tageman, B. Sadhu, J. Hallin, L. Rexberg, P. Parida, Y. Kwark, and A. Valdes-Garcia, “Development, Implementation, and Characterization of a 64-Element Dual-Polarized Phased-Array Antenna Module for 28-GHz High-Speed Data Communications,” *IEEE Transactions on Microwave Theory and Techniques*, vol. 67, no. 7, pp. 2975–2984, 2019.
- [20] J. D. Dunworth, A. Homayoun, B.-H. Ku, Y.-C. Ou, K. Chakraborty, G. Liu, T. Segoria, J. Lerdworatawee, J. W. Park, H.-C. Park, H. Hedayati, D. Lu, P. Monat, K. Douglas, and V. Aparin, “A 28GHz Bulk-CMOS dual-polarization phased-array transceiver with 24 channels for 5G user and basestation equipment,” in *2018 IEEE International Solid - State Circuits Conference - (ISSCC)*, 2018, pp. 70–72.
- [21] J. Dunworth, B.-H. Ku, Y.-C. Ou, D. Lu, P. Mouat, A. Homayoun, K. Chakraborty, A. Arnett, G. Liu, T. Segoria, J. Lerdworatawee, J. W. Park, H.-C. Park, H. Hedayati, A. Tassoudji, K. Douglas, and V. Aparin, “28GHz Phased Array Transceiver in 28nm Bulk CMOS for 5G Prototype User Equipment and Base Stations,” in *2018 IEEE/MTT-S International Microwave Symposium - IMS*, 2018, pp. 1330–1333.
- [22] A. G. Roy, O. Inac, A. Singh, T. Mukatel, O. Brandelstein, T. W. Brown, S. Abughazaleh, J. S. Hayden, B. Park, G. Bachmanek, T.-Y. J. Kao, J. Hagn, S. Dalmia, D. Shoham, B. Davis, I. Fisher, R. Sover, A. Freiman, B. Xiao, B. Singh, and J. Jensen, “A 37-40 GHz Phased Array Front-end with Dual Polarization for 5G MIMO Beamforming Applications,” in *2019 IEEE Radio Frequency Integrated Circuits Symposium (RFIC)*, 2019, pp. 251–254.
- [23] W. Hong, A. Goudelev, K.-h. Baek, V. Arkhipenkov, and J. Lee, “24-Element Antenna-in-Package for Stationary 60-GHz Communication Scenarios,” *IEEE Antennas and Wireless Propagation Letters*, vol. 10, pp. 738–741, 2011.
- [24] Y. Yin, S. Zehir, T. Kanar, and G. M. Rebeiz, “A 37-42 GHz 8x8 Phased-Array for 5G Communication Systems with 48-50 dBm EIRP,” in *2019 IEEE MTT-S International Microwave Symposium (IMS)*, 2019, pp. 480–483.

- [25] A. Natarajan, S. K. Reynolds, M.-D. Tsai, S. T. Nicolson, J.-H. C. Zhan, D. G. Kam, D. Liu, Y.-L. O. Huang, A. Valdes-Garcia, and B. A. Floyd, “A Fully-Integrated 16-Element Phased-Array Receiver in SiGe BiCMOS for 60-GHz Communications,” *IEEE Journal of Solid-State Circuits*, vol. 46, no. 5, pp. 1059–1075, 2011.
- [26] D. G. Kam, D. Liu, A. Natarajan, S. Reynolds, H.-C. Chen, and B. A. Floyd, “LTCC Packages With Embedded Phased-Array Antennas for 60 GHz Communications,” *IEEE Microwave and Wireless Components Letters*, vol. 21, no. 3, pp. 142–144, 2011.
- [27] E. Ng, Y. Beltagy, G. Scarlato, A. Ben Ayed, P. Mitran, and S. Boumaiza, “Digital Predistortion of Millimeter-Wave RF Beamforming Arrays Using Low Number of Steering Angle-Dependent Coefficient Sets,” *IEEE Transactions on Microwave Theory and Techniques*, vol. 67, no. 11, pp. 4479–4492, 2019.
- [28] N. Tervo, B. Khan, O. Kursu, J. P. Aikio, M. Jokinen, M. E. Leinonen, M. Juntti, T. Rahkonen, and A. Pärssinen, “Digital Predistortion of Phased-Array Transmitter With Shared Feedback and Far-Field Calibration,” *IEEE Transactions on Microwave Theory and Techniques*, vol. 69, no. 1, pp. 1000–1015, 2021.
- [29] X. Liu, W. Chen, L. Chen, F. M. Ghannouchi, and Z. Feng, “Linearization for Hybrid Beamforming Array Utilizing Embedded Over-the-Air Diversity Feedbacks,” *IEEE Transactions on Microwave Theory and Techniques*, vol. 67, no. 12, pp. 5235–5248, 2019.
- [30] A. B. Ayed, G. Scarlato, P. Mitran, and S. Boumaiza, “On the Effectiveness of Near-Field Feedback for Digital Pre-Distortion of Millimeter-Wave RF Beamforming Arrays,” in *2020 IEEE/MTT-S International Microwave Symposium (IMS)*, 2020, pp. 547–550.
- [31] Y. Cao, A. B. Ayed, J. Xia, and S. Boumaiza, “Uniformly Distributed Near-Field Probing Array for Enhancing the Performance of 5G Millimeter-Wave Beamforming Transmitters,” *IEEE Microwave and Wireless Components Letters*, vol. 31, no. 6, pp. 823–826, 2021.
- [32] C. A. Balanis, *Antenna Theory Analysis and Design, 3rd Edition*. Wiley, 2005.

- [33] “75 Billion IoT Devices Predicted by 2025,” Available at <https://www.achrnews.com/articles/132303-billion-iot-devices-predicted-by-->.
- [34] 3GPP, “3GPP Release 16,” Available at <https://www.3gpp.org/release-16>.
- [35] 3GPP, “3GPP Release 17,” Available at <https://www.3gpp.org/release-17>.
- [36] S.-S. Hsu, K.-C. Wei, C.-Y. Hsu, and H. Ru-Chuang, “A 60-GHz Millimeter-Wave CPW-Fed Yagi Antenna Fabricated by Using 0.18-  $\mu\text{m}$  CMOS Technology,” *IEEE Electron Device Letters*, vol. 29, no. 6, pp. 625–627, 2008.
- [37] N. Behdad, D. Shi, W. Hong, K. Sarabandi, and M. P. Flynn, “A 0.3mm<sup>2</sup> Miniaturized X-Band On-Chip Slot Antenna in 0.13 $\mu\text{m}$  CMOS,” in *2007 IEEE Radio Frequency Integrated Circuits (RFIC) Symposium*, 2007, pp. 441–444.
- [38] S. Hesami, S. R. Aghdam, C. Fager, T. Eriksson, R. Farrell, and J. Dooley, “Single Digital Predistortion Technique for Phased Array Linearization,” in *2019 IEEE International Symposium on Circuits and Systems (ISCAS)*, 2019, pp. 1–5.
- [39] N. Tervo, M. E. Leinonen, J. Aikio, T. Rahkonen, and A. Pärssinen, “Analyzing the Effects of PA Variations on the Performance of Phased Array Digital Predistortion,” in *2018 IEEE 29th Annual International Symposium on Personal, Indoor and Mobile Radio Communications (PIMRC)*, 2018, pp. 215–219.
- [40] N. Tervo, J. Aikio, T. Tuovinen, T. Rahkonen, and A. Parsinen, “Digital predistortion of amplitude varying phased array utilising over-the-air combining,” in *2017 IEEE MTT-S International Microwave Symposium (IMS)*, 2017, pp. 1165–1168.
- [41] X. Wang, Y. Li, C. Yu, W. Hong, and A. Zhu, “Digital Predistortion of 5G Massive MIMO Wireless Transmitters Based on Indirect Identification of Power Amplifier Behavior With OTA Tests,” *IEEE Transactions on Microwave Theory and Techniques*, vol. 68, no. 1, pp. 316–328, 2020.
- [42] X. Wang, C. Yu, Y. Li, W. Hong, and A. Zhu, “Real-Time Single Channel Over-the-Air Data Acquisition for Digital Predistortion of 5G Massive MIMO Wireless

- Transmitters,” in *2019 IEEE MTT-S International Wireless Symposium (IWS)*, 2019, pp. 1–3.
- [43] X. Liu, Q. Zhang, W. Chen, H. Feng, L. Chen, F. M. Ghannouchi, and Z. Feng, “Beam-Oriented Digital Predistortion for 5G Massive MIMO Hybrid Beamforming Transmitters,” *IEEE Transactions on Microwave Theory and Techniques*, vol. 66, no. 7, pp. 3419–3432, 2018.
- [44] A. Brihuega, M. Abdelaziz, L. Anttila, M. Turunen, M. Allén, T. Eriksson, and M. Valkama, “Piecewise Digital Predistortion for mmWave Active Antenna Arrays: Algorithms and Measurements,” *IEEE Transactions on Microwave Theory and Techniques*, vol. 68, no. 9, pp. 4000–4017, 2020.
- [45] A. Agrawal and A. Jablon, “A calibration technique for active phased array antennas,” in *IEEE International Symposium on Phased Array Systems and Technology, 2003.*, 2003, pp. 223–228.
- [46] A. Ben Ayed, Y. Cao, P. Mitran, and S. Boumaiza, “Digital Predistortion of Millimeter-Wave Arrays Using Near-Field Based Transmitter Observation Receivers,” *IEEE Transactions on Microwave Theory and Techniques*, vol. 70, no. 7, pp. 3713–3723, 2022.
- [47] J. OuYang, F. Yang, and Z. M. Wang, “Reducing Mutual Coupling of Closely Spaced Microstrip MIMO Antennas for WLAN Application,” *IEEE Antennas and Wireless Propagation Letters*, vol. 10, pp. 310–313, 2011.
- [48] Y. Hajilou, H. R. Hassani, and B. Rahmati, “Mutual coupling reduction between microstrip patch antennas,” in *2012 6th European Conference on Antennas and Propagation (EUCAP)*, 2012, pp. 1–4.
- [49] M. M. Bait-Suwailam, O. F. Siddiqui, and O. M. Ramahi, “Mutual Coupling Reduction Between Microstrip Patch Antennas Using Slotted-Complementary Split-ring Resonators,” *IEEE Antennas and Wireless Propagation Letters*, vol. 9, pp. 876–878, 2010.

- [50] G. Expósito-Domínguez, J. M. Fernández-González, P. Padilla, and M. Sierra-Castañer, “New EBG solutions for mutual coupling reduction,” in *2012 6th European Conference on Antennas and Propagation (EUCAP)*, 2012, pp. 2841–2844.
- [51] C.-C. Hsu, K.-H. Lin, and H.-L. Su, “Implementation of Broadband Isolator Using Metamaterial-Inspired Resonators and a T-Shaped Branch for MIMO Antennas,” *IEEE Transactions on Antennas and Propagation*, vol. 59, no. 10, pp. 3936–3939, 2011.
- [52] A. Nafe, K. Kibaroglu, M. Sayginer, and G. M. Rebeiz, “An In-Situ Self-Test and Self-Calibration Technique Utilizing Antenna Mutual Coupling for 5G Multi-Beam TRX Phased Arrays,” in *2019 IEEE MTT-S International Microwave Symposium (IMS)*, 2019, pp. 1229–1232.
- [53] L. Liu, W. Chen, L. Ma, and H. Sun, “Single-PA-feedback digital predistortion for beamforming MIMO transmitter,” in *2016 IEEE International Conference on Microwave and Millimeter Wave Technology (ICMMT)*, vol. 2, 2016, pp. 573–575.